Spring 2017

A 3D Framework for Characterizing Microstructure Evolution of Li-Ion Batteries

Jeffrey David Gelb
San Jose State University

A 3D FRAMEWORK FOR CHARACTERIZING MICROSTRUCTURE EVOLUTION OF LI-ION BATTERIES

A Thesis

Presented to

The Faculty of the Department of Biomedical, Chemical, and Materials Engineering

San José State University

In Partial Fulfillment

of the Requirements for the Degree

Master of Science

by

Jeffrey Gelb

May 2017

The Designated Thesis Committee Approves the Thesis Titled

A 3D FRAMEWORK FOR CHARACTERIZING MICROSTRUCTURE EVOLUTION OF LI-ION BATTERIES

By

Jeffrey Gelb

APPROVED FOR THE DEPARTMENT OF BIOMEDICAL, CHEMICAL, AND MATERIALS ENGINEERING

SAN JOSÉ STATE UNIVERSITY

May 2017

Dr. Melanie McNeil	Department of Biomedical, Chemical, and Materials Engineering
Dr. Craig England	Department of Biomedical, Chemical, and Materials Engineering
Dr. Arno Merkle	Senior Manager, Carl Zeiss Microscopy

ABSTRACT

A 3D FRAMEWORK FOR CHARACTERIZING MICROSTRUCTURE EVOLUTION OF LI-ION BATTERIES

by Jeffrey Gelb

Lithium-ion batteries are commonly found in many modern consumer devices, ranging from portable computers and mobile phones to hybrid- and fully-electric vehicles. While improving efficiencies and increasing reliabilities are of critical importance for increasing market adoption of the technology, research on these topics is, to date, largely restricted to empirical observations and computational simulations. In the present study, it is proposed to use the modern technique of X-ray microscopy to characterize a sample of commercial 18650 cylindrical Li-ion batteries in both their pristine and aged states. By coupling this approach with 3D and 4D data analysis techniques, the present study aimed to create a research framework for characterizing the microstructure evolution leading to capacity fade in a commercial battery. The results indicated the unique capabilities of the microscopy technique to observe the evolution of these batteries under aging conditions, successfully developing a workflow for future research studies.

ACKNOWLEDGEMENTS

The author gratefully acknowledges the help and support of University College London's Electrochemical Innovation Laboratory, with special thanks to Dr. Donal Finegan, Dr. Paul Shearing, and Prof. Dan Brett for their participation in the battery aging experiments. The support of Carl Zeiss X-ray Microscopy is also gratefully acknowledged for the access to imaging instrumentation and financial support throughout the course of this research. Furthermore, the author wishes to thank Dr. Craig England, Prof. Melanie McNeil, and Prof. Guna Selvaduray (San José State University) as well as Dr. Arno Merkle (Carl Zeiss Microscopy) and Dr. Stephen Harris (Lawrence Berkeley National Laboratory) for many engaging and enlightening conversations about this research project and the research process in general.

Finally, the author wishes to thank his wife Yuliana, son Tyler, and parents Fran and Jack Gelb for their endless motivation, patience, love, and general support throughout the course of this research and the coursework preceding it. He further wishes to acknowledge his late grandfather John Jewell Burner, who taught him that "an education is worth more than gold." To his dear family, and his loving grandfather, this one is for you.

TABLE OF CONTENTS

LIST OF TABLES

LIST OF FIGURES

CHAPTER ONE
INTRODUCTION

1.1 Significance

In the present day, the need for energy storage devices is in a state of rapid expansion. From stationary devices for storage of energy from renewable sources to portable solutions for consumer electronics, the need for controlled energy storage and release mechanisms is a vital component of the modern world. While many primary (single charge) and secondary (rechargeable) energy storage solutions are available, lithium-ion (Li-ion) secondary batteries are of key interest, due to their high output properties, fast charging capabilities, and durability in a wide range of environments [1]. These properties are particularly attractive for a variety of applications, and Li-ion batteries are being increasingly adopted as a result, with exponential growth expected over the next decade [2].

Much of this need is currently sourced from the automotive industry, with consumers turning toward hybrid and fully electric vehicles to combat rising fuel prices and to suit their transportation needs. According to a recent survey by JD Power Global Forecasting, the global demand for hybrid- and plug-in hybrid electric vehicles is expected to reach close to a 6% market share of total vehicle sales by 2020, approaching annual sales of nearly 4,000,000 units [3]. The market breakdown of battery- and plug-in-hybrid electric vehicles (BEVs and PHEVs, respectively), has been found to be rooted primarily in the US and Japan, with China and many European nations trailing close behind [4].

In a recent report by a major international research organization, several key opportunities were identified for enhancing market growth [4]. The report detailed the need for reducing battery costs while simultaneously increasing capacities, in order to meet market demands and support the proliferation of EVs [4]. In parallel with this, engineers must be conscious of maintaining safety and reliability standards, both in the interest of keeping consumers safe and reducing long-term costs of ownership, while also investigating novel battery designs to increase battery efficiencies [4]. From this report, it was clear that, while the substantial growth in adoption of battery-powered vehicles is on the horizon, some significant work is needed by engineers worldwide to support the development of battery (and, consequently, EV) technologies.

1.2 Motivation

Due to the substantial influx of battery-powered vehicles, it is consequently of increasing importance to understand the failure modes of the batteries, in order to ensure the safety and satisfaction of the consumers. Failures may range from simple nuisances, such as poor vehicle ranges and the need for frequent charging, to failures with more catastrophic consequences, such as short circuits, venting, and fires. For this reason, it is now more than ever critical to understand the characteristics of the battery cells that lead to failure, so that the failure frequency may be reduced and ultimately avoided.

In spite of the known consequences of battery failure, there remains a poor understanding of what aspects of battery cells dictate performance and, thus, degradation. The latest research into battery performance characteristics is now turning to their microstructure, as will be described in detail within the following sections. Much of this

work hinges on classical theory linking microstructural properties to transport characteristics. In 1935, Von D. A. G. Bruggeman published a theoretical result that linked porosity to tortuosity, resulting in the famous "Bruggeman Relation" that states an inverse exponential relationship between porosity (ϵ, a microstructural parameter) and tortuosity (τ, a transport parameter), described in Equation 1 [5].

$$\tau = \frac{1}{\epsilon^{0.5}} \qquad \text{Equation 1}$$

As battery technology flourished many years later, the Bruggeman relationship was subsequently used in the design of electrode microstructures, in order to relate the pore frequency to transport geometry. However, suitable techniques for characterizing the electrodes had not been developed, and thus the practical application of the Bruggeman relationship was implemented without rigorous validation for the Li-ion battery material system.

It took many decades later, with the advent of X-ray computed tomography (CT) characterization instruments, for the actual electrode geometries to be properly characterized. In 2010, Shearing *et al.* used micro-CT technology to characterize a commercial battery electrode, revealing the actual pore networks in 3D [6]. This experiment demonstrated the power of 3D imaging to directly characterize the electrode microstructure, in order for future experiments to verify the link between microstructure and transport properties. Since that time, there has been a flurry of activity on the subject, notably in the year following when Kehrwald *et al*. performed a simulation study to show the impact of local microstructure heterogeneities (tortuosity) on cell performance [7]. Two years later, Ebner and collaborators published the first high-

visibility study linking microstructural defects to Li-ion battery failure, pointing to the need for 3D characterization in order to properly predict battery cell performance [5]. The timeline for these developments is illustrated in Figure 1.

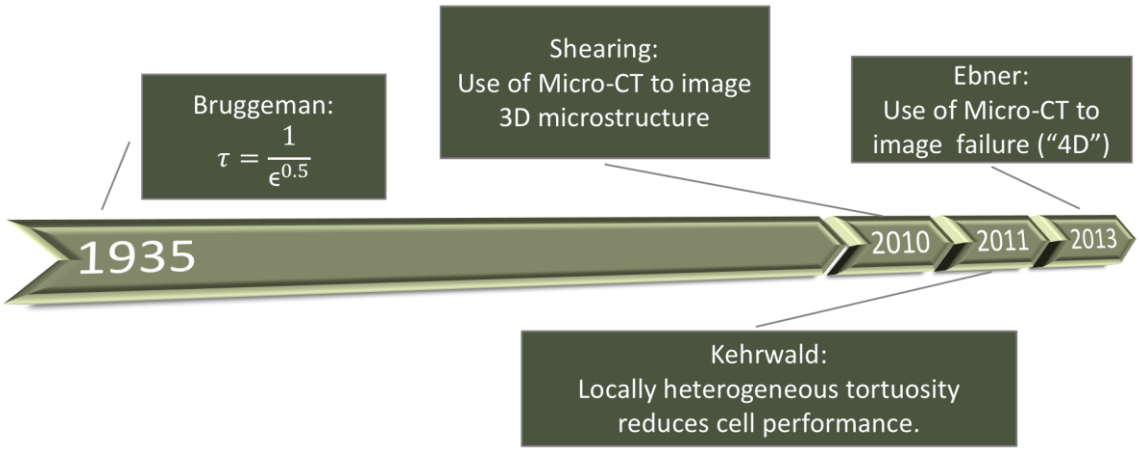

Figure 1. Timeline of developments linking battery microstructure to cell performance.

At the present time, there remains little more information on the degradation mechanisms for Li-ion battery cells, which the present study aims to rectify. Within the scope of the present study, modern 3D X-ray microscopy will be employed to directly, and non-destructively, probe the nucleation and propagation of defects within a packaged commercial Li-ion cylindrical secondary battery cell. These will be related to the charge/discharge rates, as well as the cycle lifetime of the cells.

CHAPTER TWO
LITERATURE REVIEW

The Li-ion battery research landscape is one that has been marked by several notable achievements throughout the years. Here, a brief history of the development of Li-ion batteries is initially presented. This is followed by a discussion of research trends, in particular reviewing microstructure-based research in recent years. The microstructure research has been supported by several novel characterization techniques, which will also be presented in the context of Li-ion battery research.

2.1 Terminology and Battery Design

Batteries are electrochemical energy storage devices, capable of dispensing charge via electron flow, facilitated by oxidation-reduction reactions. Prior to discussing the technology itself, however, a quick note about terminology is warranted. Commercial battery products are commonly available, and manufacturers and consumers alike often use the term *battery* and *cell* interchangeably. In reality, a *cell* is the basic unit of electrochemical energy storage – it consists of defined components (discussed next), and on its own is capable of delivering current flow via conversion of chemical energy on demand. The cell may take on a range of geometries depending on desired form factor, such as cylindrical, prismatic, button, or flat form factors. A *battery*, on the other hand, may consist of several such cells working together, for example wired in series or parallel, to produce a final product capable of serving the intended application. The battery may also include various monitoring circuits, such as protective fuses and switches, which aid in the performance after integration. Batteries may be designed with *primary* cells, which produce an irreversible reaction permitting a single charge-

discharge cycle only, or *secondary* cells, where the reversibility of the electrochemical reaction allows the batteries to be "recharged" and used for multiple charge cycles [1].

The basic battery cell consists of two electrodes, electronically isolated from each other, and an electrolyte that facilitates ionic transport. One electrode is responsible for the reduction reactions and is oxidized during operation, thus freeing electrons to move through a circuit and do work. This electrode is commonly called the *anode*, or, more specifically, the *negative electrode*. The other electrode attracts the freed electrons and is reduced during operation; this *positive electrode* is more commonly called the *cathode*. Each electrode is fabricated on a metal foil, called the *current collector*, which is responsible for collecting the freed electrons and transporting them to the *terminals*. A circuit may be subsequently connected to the terminals, where the electrons do work and are then transported back to the other electrode to complete the electrochemical reaction. Electrolytes are ionic-conducting media, capable of ionic transport but electronically nonconductive (to avoid short-circuits inside the cell). They are typically aqueous salt solutions, designed to be inexpensive, stable under a variety of conditions, and nonreactive with the electrochemically active materials. In addition to these layers, often a mechanical separation is introduced between electrodes by a medium called the *separator*. This material may be permeable to the electrolyte, but should keep the electrodes safely isolated from each other, again to avoid short circuits [1].

2.2 Battery Materials

2.2.1 Material Requirements

Many materials have been proposed in the past for battery cells, each with unique advantages and disadvantages. Anode materials are generally selected based on several design considerations: "efficiency as a reducing agent, high columbic output, good conductivity, stability, ease of fabrication, and cost" [1]. Cathode materials are designed to be efficient oxidizing agents, working in concert with the electrolyte without undesired reactions, and be capable of producing a voltage within the desired range [1]. The materials should also be as light in weight as possible, to enable portability in their final service applications [1]. These general characteristics have lead a variety of specific cell compositions, ranging from Pb-based to Ni, Zn, and Cd-based chemistries [1,8].

2.2.2 The Rise of Lithium

In the early 1970s, it was demonstrated that lithium, the most electropositive metal, and very light in weight, was capable of serving as a promising material for a functioning cell [8]. Cells based on Li chemistry grew in favor, due to their "high capacity and variable discharge rate," and quickly found applications for small-scale portable devices (ranging from calculators and watches to implantable medical devices) [8]. The many advantages of Li-ion batteries represented important capabilities for modern devices, as summarized in Table 1. With the development of various intercalation compounds, Li-ion batteries rapidly developed into materials that could deliver high energy densities, both light in weight and small in size, as shown in Figure 2 [8,9]. These advantages were largely responsible for the wide-scale adoption experienced by Li-ion battery technology

over the past several decades, and have been credited for the growth of portable consumer device technologies, such as laptop computers and mobile phones [9].

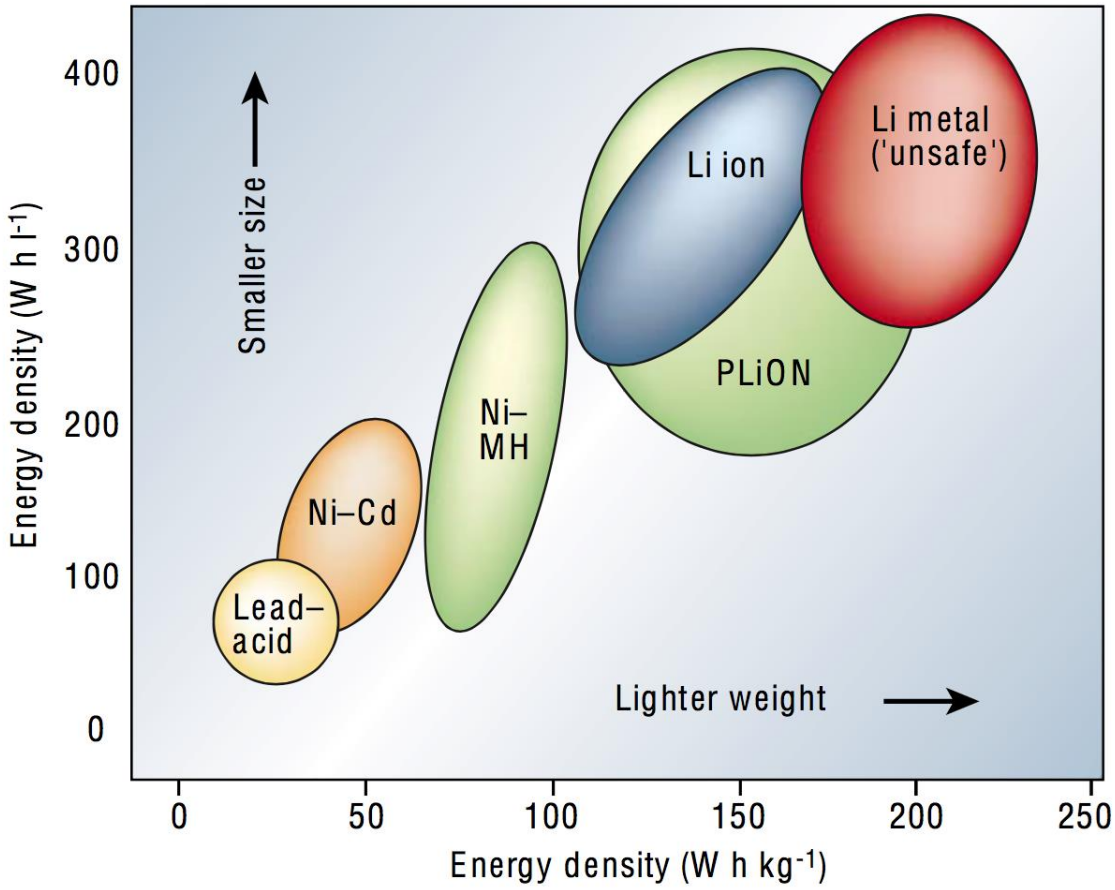

Figure 2. Comparing the volumetric energy density to the gravimetric energy density for a variety of battery materials. Li-ion batteries have been demonstrated to produce suitably high energy densities, while minimizing both size and weight of the cells [8]. Reprinted by permission from Macmillan Publishers Ltd: Nature [8], copyright 2001.

Table 1. Summary of the Advantages and Disadvantages of Li-ion Batteries as Compared to Other Cell Chemistries [1]

Advantages	*Disadvantages*
Sealed cells, no maintenance required	Moderate initial cost
Long cycle life	Degrades at high temperature
Broad temperature range of operation	Need for protective circuitry
Long shelf life	Capacity loss or thermal runaway when overcharged
Low self-discharge rate	Venting and possible thermal runaway when crushed
Rapid charge capability	Cylindrical designs typically offer lower power density than NiCd or NiMH
High rate and high power discharge capability	
High columbic and energy efficiency	
High specific energy and energy density	
No memory effect	

2.2.3 Cell Design

A typical Li-ion contains a negative electrode typically fabricated from graphite, a positive electrode formed from a lithium metal oxide (such as $LiCoO_2$), and a lithium salt electrolyte in an organic solvent (such as ethylene carbonate-dimethyl carbonate, or EC-DMC) [9]. The electrodes are deposited onto current collecting foils, typically copper for the negative electrode and aluminum for the positive electrode, as shown in Figure 3 [9]. The raw materials are formed into particles, which are coated onto the foils and then pressed (*calendared*) to reach the desired electrode thickness [10].

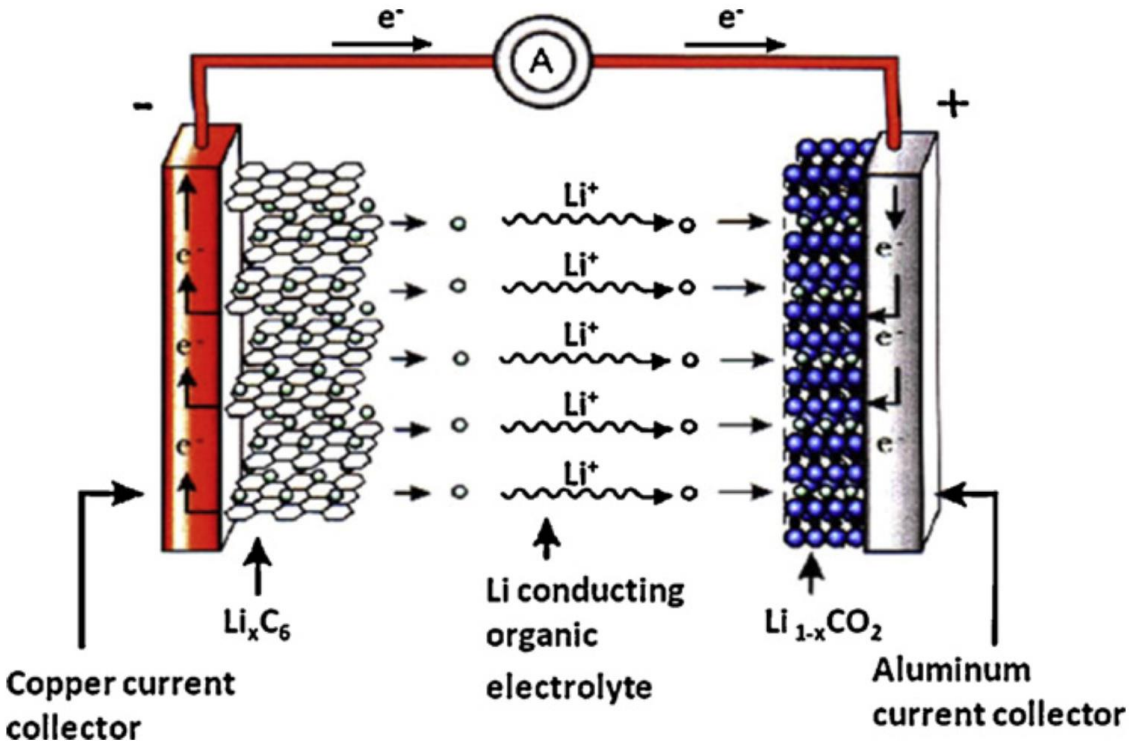

Figure 3. Schematic representation of a typical Li-ion battery. The negative electrode is typically graphite deposited onto a copper current collector, while the positive electrode (lithium metal oxide) is deposited onto an aluminum current collector. Lithium ions transfer through the EC-DMC electrolyte [9]. Reprinted from Journal of Power Sources, 195/9, Scrosati & Garche, Lithium Batteries: Status, Prospects and Future, pp. 2419-2430, Copyright 2010, with permission from Elsevier.

2.3 Effect of Defects on Cell Performance: Computational Simulations

In spite of the growth and wide-scale adoption of Li-ion battery technologies, there exists a relatively small amount of documentation in the literature about microstructure and the role of defects in operation. As pointed out in the literature, one of the major gaps limiting the proliferation of Li-ion batteries is the need for characterization of microstructure – in particular, the evolution of microstructure – in order to better understand the operation of the batteries at their fundamental levels [8].

2.3.1 Positive Electrodes

Many initial studies in recent years were performed using computational simulations on the particle level, to use fundamental theory to predict the properties of the materials. The Newman group at UC Berkeley was responsible for some of the initial modeling, which showed that higher power applications with higher charge/discharge rates results in higher stresses in the positive electrode particles [11]. This was the result of modeling lattice expansion in the metal oxide under intercalation of an insertion material, e.g., Li^+, with a high rate of diffusion and high concentration gradient, and suggests that applications with demanding power requirements may experience larger stresses and, correspondingly, a higher tendency to fracture [11]. However, the Newman models assumed spherical particles, which represented an idealistic viewpoint of the manufactured battery products. Zhang *et al.* applied this model to the $LiMn_2O_4$ system of positive electrode particles and modeled the diffusion-induced stresses, which were believed to occur during lithiation/delithiation [12]. They confirmed that, for their specific material system, a similar coupling between high charge/discharge rates and large intraparticle stresses exists for both spherical and nonspherical particles alike [12]. In the same report, Zhang *et al.* examined ellipsoidal particles of nonspherical morphology and found that higher aspect ratios reduced some of the mechanical stresses induced by the Li^+ intercalation [12], suggesting that high aspect ratio particles may have some advantages for high power applications.

To explain the process behind the intercalation-induced stresses, Zhao *et al.* examined the fracture behavior of negative electrode particles in the conditions of rapid

charging [13]. The results of their research showed that a "fast" charge represents a case where the Li^+ is not given sufficient time to reach a homogeneous distribution within the diffusion couple, producing an inhomogeneous distribution that leads to local stresses in the particle lattice [13]. These stresses were found to drive defects, ultimately resulting in failure nucleation sites and fractures [13]. Their results provide a framework for predicting so-called "critical rates" for charging a Li-ion battery, dependent on chemistry and microstructure, based on the fundamentals of fracture mechanics and diffusion kinetics [13]. This work was performed in tandem with that of Woodford *et al.*, who looked at rapid charging of Li-ion battery positive electrodes also from a fracture mechanics perspective, in a state of "electrochemical shock" [14]. The report detailed the condition of pre-existing voids (e.g., manufacturing defects) and related the rapid growth of cracks above a critical charging rate to the cracks already present in the electrode [14]. Woodford *et al.* also found that large particles produce correspondingly low critical charging rates, suggesting that smaller particles may be more resistant to defect nucleation & propagation [14]. Comprehensive Li-diffusion [15] and crack-initiation [16] models have more recently been reported, but a complete description of these models is beyond the scope of the current discussion.

2.3.2 Negative Electrodes

Similar modeling / simulation work has been performed on the negative electrode, but is perhaps more limited in abundance. Toyota Motor Corporation, in collaboration with Lawrence Berkeley National Laboratory, examined the cracking of graphite negative electrodes as a function of cycling rates, using measured diffusivities and

computational simulations [17]. The results of their findings suggested that, for a typical Li-ion battery in a typical vehicular application, cracking of the negative electrode particles is unlikely to occur, even at very high charge/discharge rates [17]. Perhaps the most significant cases of negative electrode fracture/failure is that reported in novel chemistries, such as the case of Si electrodes, where the volumetric expansion may be upwards of 300% for a typical lithiation process [18]. This has been studied via finite element simulations [18] and also directly observed experimentally on Sn-based electrodes [19-21], as discussed in the following section.

2.4 Li-Ion Battery Characterization with Imaging

2.4.1 3D Image-Based Characterization

Recent advancements in Li-ion battery technology have benefitted from parallel advancements in available characterization techniques. Modern imaging instrumentation, such as X-ray microscopes (XRMs), are now enabling 3D studies of porous electrode materials with resolutions down to the tens of nanometers [22], producing high-resolution representations of the material microstructures. This technique works on the principles of computed tomography, where the specimen is rotated about a central axis, pausing at discrete intervals to collect X-ray projection radiographs; these projection radiographs are subsequently reconstructing using a Feldkamp-David-Kress (FDK) or filtered back-projection reconstruction algorithm to produce a 3D representation of the specimen's microstructure [22,23]. The XRM technique is rapidly becoming adopted, with several dozen publicly-accessible sites available worldwide, as shown in Figure 4 [24].

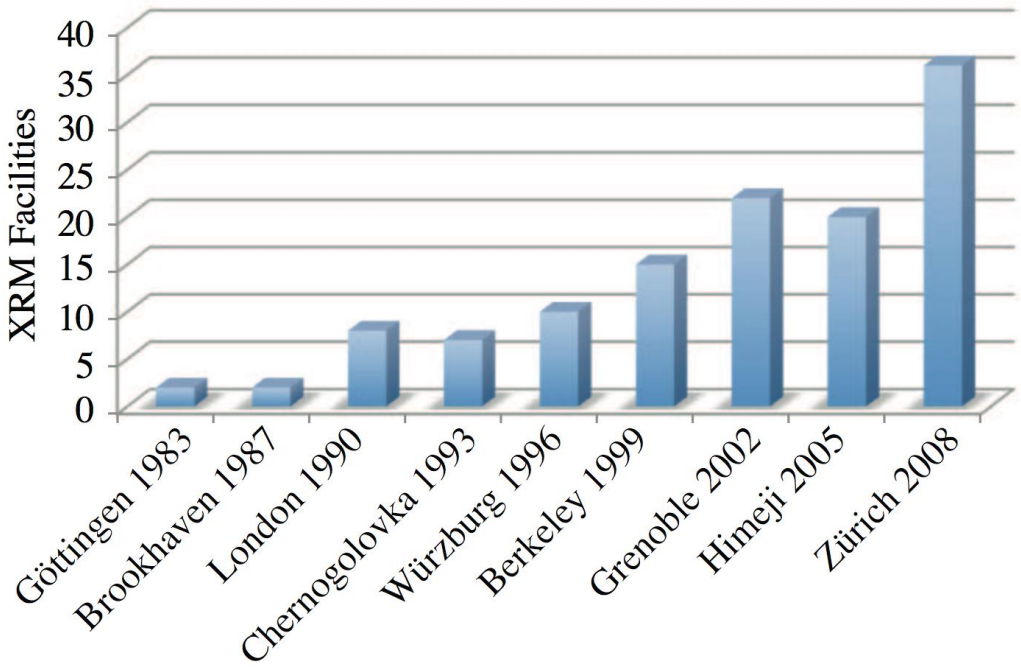

Figure 4. Number of available XRM facilities, as reported at the periodic X-Ray Microscopy Conference [24].

Applications of XRM for Li-ion battery research have grown in popularity in recent years, as researchers have begun utilizing the unique strengths of the technique to understand the 3D structure of the cells and electrodes. Amongst the most prolific of researchers in this regard is Dr. Paul Shearing, who has published several papers using the XRM technique for Li-ion battery characterization. Shearing *et al.* used multi-length scale XRM to characterize a commercial Li-ion battery cathode, in which it was determined that the single-micron length scale is appropriate for understanding bulk particle assembly and general pore geometry, with the nano-scale imaging reserved for precise pore morphologies and intraparticle defect analysis, as shown in Figure 5 [25]. Contrary to previous reports [26], where polarization-interrupt and AC-impedance

spectroscopy were used to indirectly extract the tortuosity of the pore networks, XRM has been shown to provide a direct means of accessing the 3D microstructure of Li-ion batteries via imaging [6,25,27].

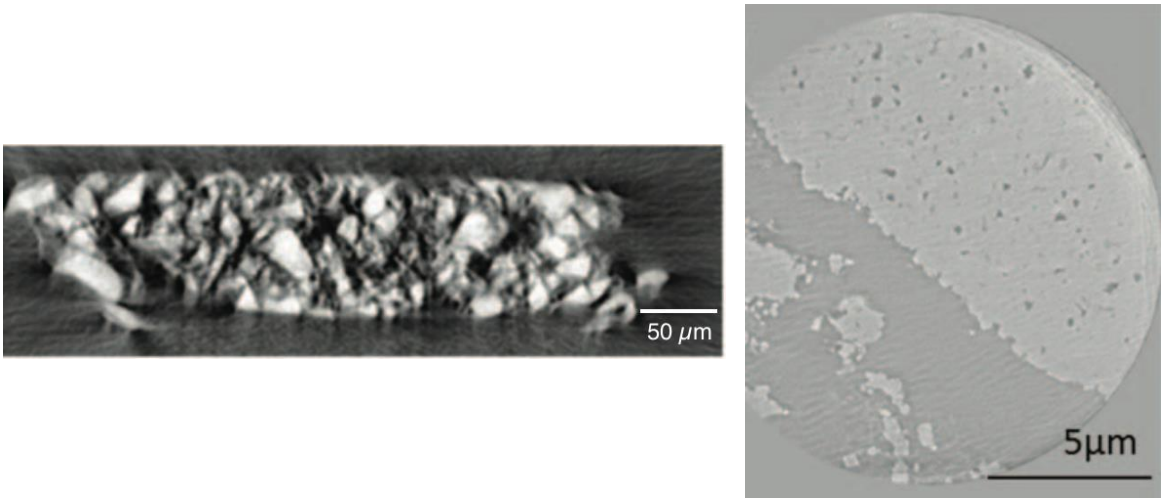

(a) (b)

Figure 5. Virtual slices from 3D volumes of XRM data, with (a) micron-scale and (b) nano-scale resolution. The micron-scale data shows the particles (white) and pores (black), while the nano-scale data shows defects (black) within a single particle (light grey) [25]. Reproduced by permission of The Electrochemical Society.

Several recent research projects have focused on applying nano-scale XRM to map both the structure [19,21,28-36] and chemistry [29,37-39] of Li-ion batteries, but these reports have primarily focused on high-resolution studies of single particles, rather than the functioning electrochemical system of a battery cell. There are, however, a few reports [5,6,34,40-44] of using the XRM technique to characterize the 3D meso-structure of a functioning Li-ion battery, which are subsequently discussed. In the work of Harris *et al.* [45] and Kehrwald *et al.* [7], as two examples, the 3D structure of particle assemblies were considered, in an effort to utilize the measured pore geometry in ionic transport simulations to predict electrochemical reaction rates for a particular cell design.

Kehrwald *et al*. examined a battery electrode using the XRM technique and compared the results to those predicted via computer simulation. According to the Bruggeman Relation, shown in Equation 1, a direct relationship exists between the porosity, or volume fraction of pore space within the specimen, and tortuosity, a measure of the deviations of the pore pathway from a straight line [5]. Based on the 3D imaging results achieved via XRM, the researchers found a substantial disagreement (deviation) between the simulation results and actual measured results, as shown in Figure 6 [7]. This result suggested that the Bruggeman Relation may represent more of an average result, without taking into account the local variations in ionic transport pathways. This showed that the assumptions made by Newman and others may indeed neglect local inhomogeneities within the pore network. These local variations may represent defect sites, where, for example, Li plating may occur, leading to a reduction in capacity [7]. The local variations reported by Kehrwald *et al.* were confirmed by Harris *et al.*, who showed a similar series of local inhomogeneities on a graphite electrode, as shown in Figure 7 [45]. By extension, any battery that incorporates defects likewise incorporates local inhomogeneities, which ultimately will affect the performance of the battery product. Thus, 3D image-based characterization may represent a novel insight into the degradation and failure mechanisms of Li-ion batteries, suggesting that XRM may be a highly beneficial approach toward gaining a better understanding of the 3D morphology (and real-life performance characteristics) of the batteries.

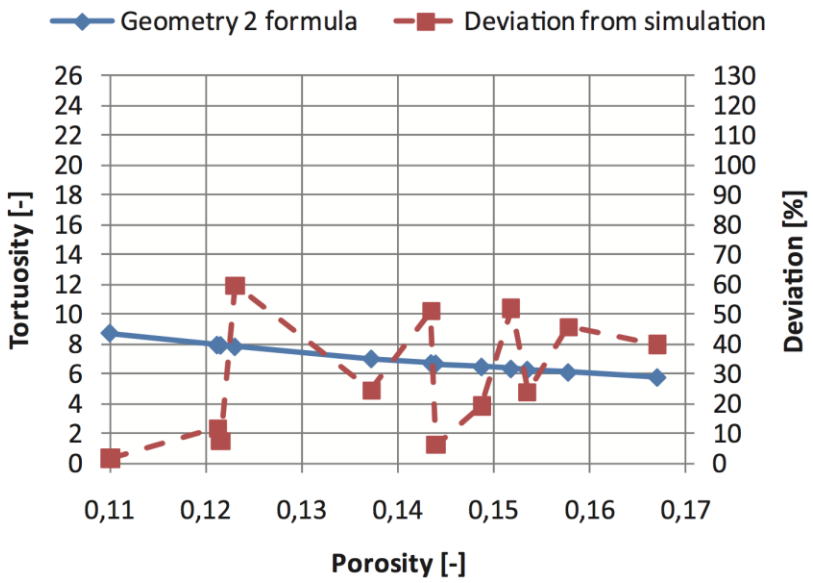

Figure 6. Computer simulation results have been found to be quite different from actuality, with the Bruggeman Relationship representing more of a global average coupling between porosity and tortuosity [7]. Reproduced by permission of The Electrochemical Society.

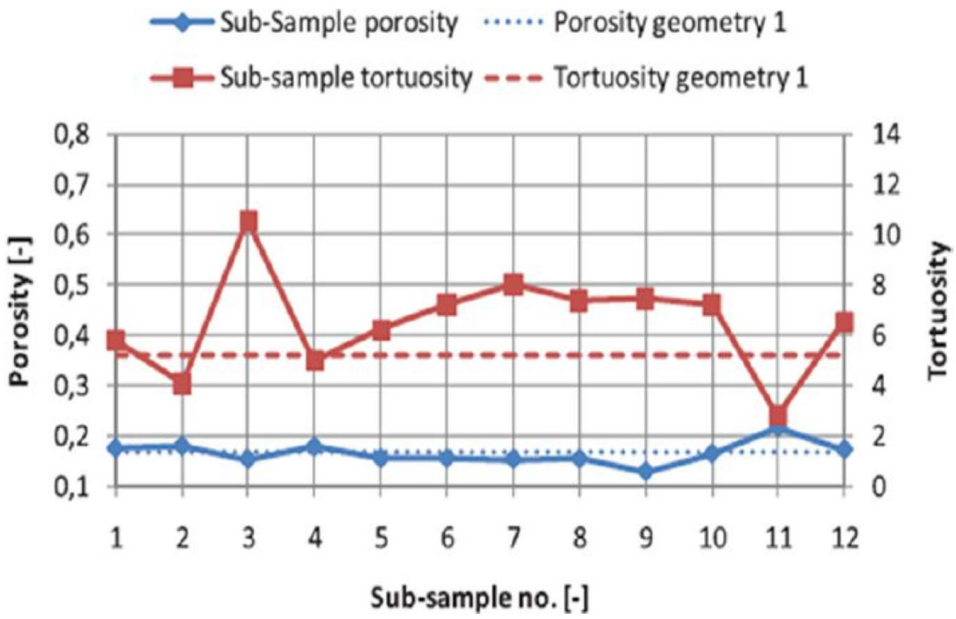

Figure 7. By virtually splitting the XRM volume into several sub-sampled datasets, the variations in porosity and tortuosity were revealed [45]. Reprinted with permission from [45]. Copyright 2013 American Chemical Society.

2.4.2 Microstructure Evolution and 4D Characterization

One of the unique advantages of XRM is the non-destructive nature of the imaging technique. This allows for studies beyond static 3D information, but paves the way for studies of microstructure evolution, a so-called "4D" characterization protocol. Haibel *et al*. used synchrotron-hosted XRM to examine the discharge processes within a AAAA alkaline cell, in which the deoxidation of the manganese dioxide to manganite was observed, as well as a dissolution and oxidation of the Zn particles in the negative electrode [40]. This provided valuable information about the 4D evolution of alkaline microstructure, but applies, at best, indirectly to Li-ion battery chemistries. As shown in Figure 8, Ebner *et al.* used synchrotron-hosted XRM at the micron scale to visualize and quantify the evolution processes within a Sn-based Li-ion battery, revealing the initiation of cracks and defects within the particles [5]. While also providing valuable information about the battery evolution, namely the observation of defect formation and propagation with charge cycling, the study was restricted to Sn-based chemistries, which are not yet in widespread adoption and may not accurately represent a commercial Li-ion battery.

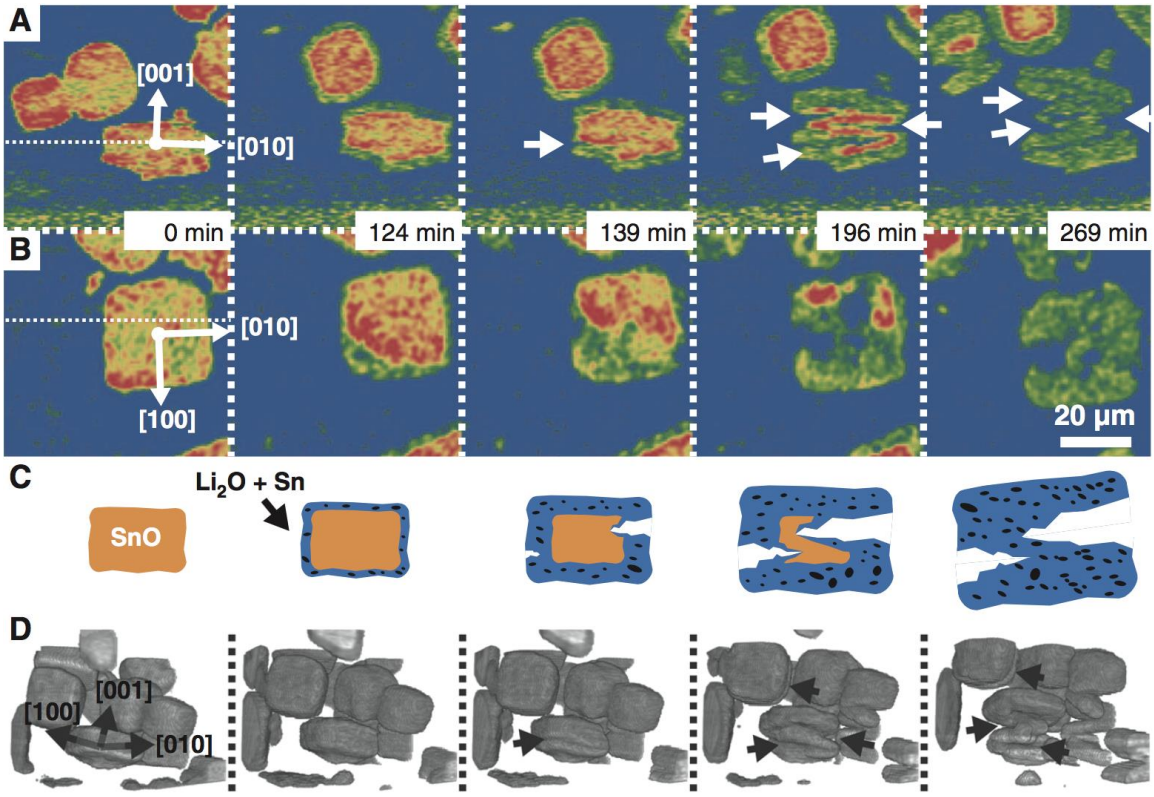

Figure 8. Evolution of a Sn battery electrode over time, with arrows indicating the development of cracks. Views from the (a) coronal and (b) transverse virtual slicing directions are shown, along with (c) a schematic drawing to illustrate the process and (d) a 3D volume rendering. From [5]. Reprinted with permission from AAAS.

In the work of Eastwood *et al.*, a commercial coin-cell type Li-ion battery was used for laboratory micro-XRM investigation [43]. The battery under investigation was a Panasonic ML414, about 5mm in diameter, and XRM results of the interior microstructure are shown in Figure 9 [43]. By imaging the battery before and after charge cycling, the report details the use of digital volume correlation to map the particle dilation processes associated with charge cycling, showing a positional dependence of volumetric expansion resulting from charging and displayed in Figure 10 [43]. Further analysis of the data, shown in Figure 11, revealed that the closer each particle was to the

terminal, the more the particle was observed to dilate when the battery was charged [43] – those particles that were farther away from the terminal did not exhibit substantial dilation, suggesting that such particles may have been electrochemically inactive [43]. This exemplified how modern imaging and data analysis techniques may be used together for a better understanding of Li-ion battery microstructure evolution as applied to a commercial product, but focuses on a specialized coin cell geometry, which may not entirely represent some of the more common Li-ion battery assemblies.

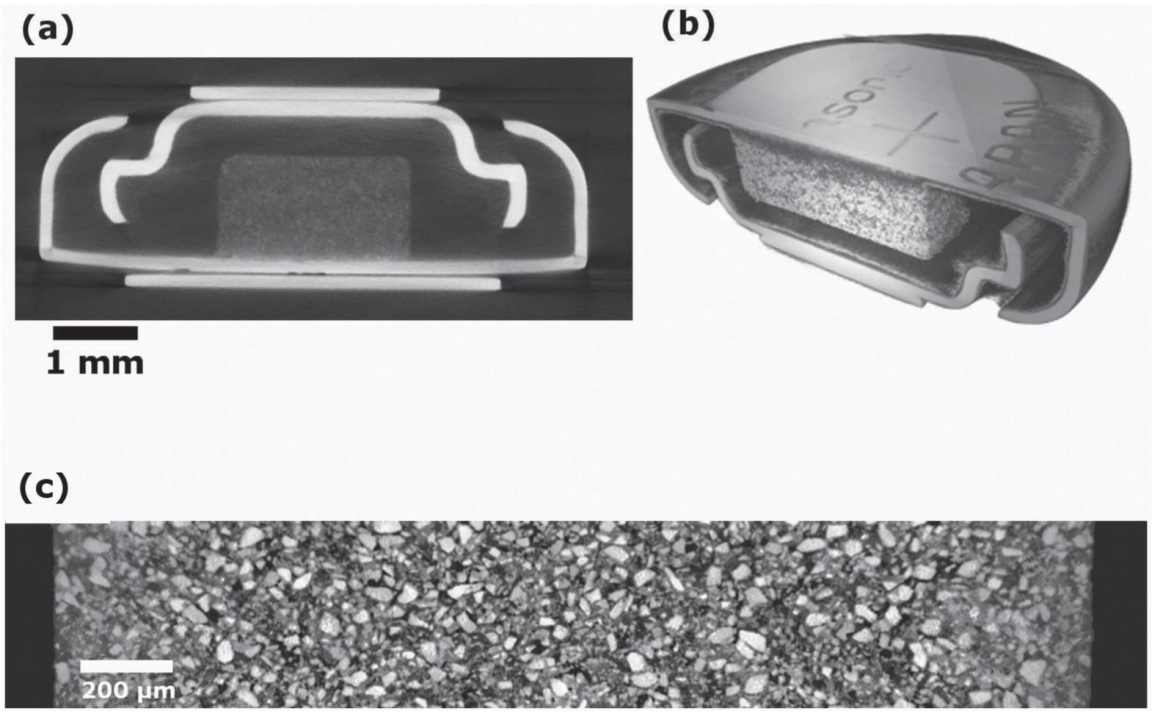

Figure 9. The XRM images of the small coin cell Li-ion secondary battery is shown here, as (a) transverse virtual slice, (b) 3D rendering of the battery virtually sectioned, and (c) a transverse virtual slice through the active material [43]. © 2013 WILEY-VCH Verlag GmbH & Co. KGaA, Weinheim. Reprinted with permission.

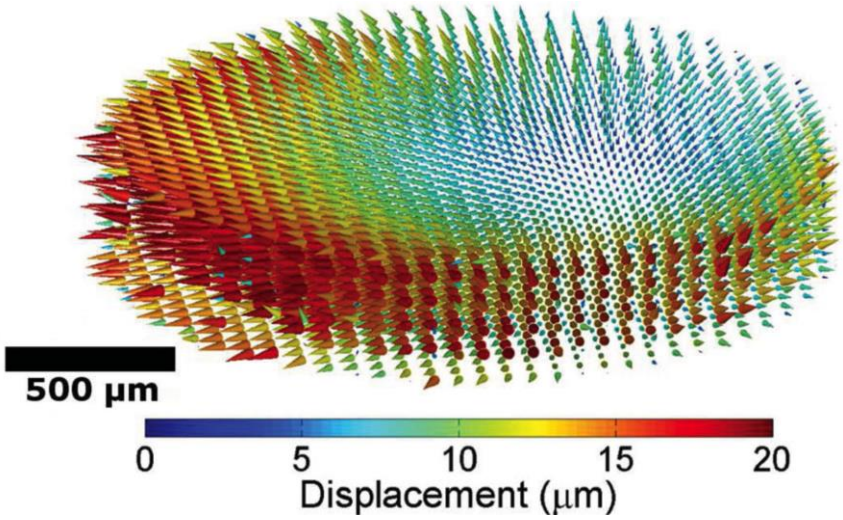

Figure 10. Results from the digital volume correlation analysis on the ML414, showing a positional dependence of particle dilation in a single charge cycle [43]. Reprinted with permission. © 2013 WILEY-VCH Verlag GmbH & Co. KGaA, Weinheim. Reprinted with permission.

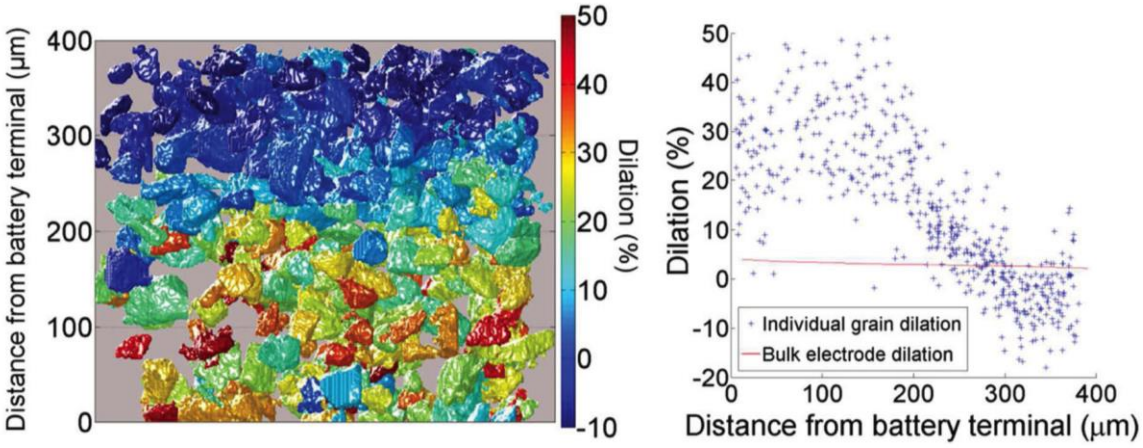

Figure 11. The particle dilation was found to be a function of the distance between each particle and the terminals, suggesting that, in this particular battery, only about half of the material was electrochemically active [43]. © 2013 WILEY-VCH Verlag GmbH & Co. KGaA, Weinheim.

2.5 Summary

Modern Li-ion batteries represent the culmination of decades of innovation and development. They offer many advantages over traditional batteries and, as a result, have become critical components of many present-day consumer devices. The literature contains a growing library of data with regard to computer simulations of battery operation and failure, which is supported by imaging studies of actual battery microstructure. With the advent of non-destructive 3D imaging techniques, such as XRM, some specific microstructure evolution processes have been documented, showing significant discrepancies between predicted and empirically-derived properties. This has pointed to potential issues with the fundamental models of Li-ion batteries, suggesting that further work should be done to identify and characterize cell failure. While some studies have indeed been performed, they have focused primarily on particle-scale changes, leaving a gap in the literature with regard to cell- and battery-scale evolution as a result of operation.

CHAPTER THREE
RESEARCH OBJECTIVE

3.1 Research Landscape

While considerable work has been done in both modeling and experiment to understand the microstructure-based failures of Li-ion batteries, still little has been done to look at bulk defect formation and large-scale device failures. Much of the recent work has been focused on particle-level defects in quasi-idealized environments. There remains a gap in the current body of research to extend the results of the previous reports from the particle scale to that of practical, commercial battery products, to understand how batteries in consumer devices perform and fail. Some work has been done to model the lifetime of a Li-ion battery in, for example, electric vehicle applications [46], but the work is both limited in scope and makes several assumptions about both composition and microstructure, thus neither as descriptive nor comprehensive as what may be achieved via direct image-based characterization.

3.2 Objectives and Hypotheses

The aim of this project is to build a framework for characterizing the failure and degradation mechanisms of a Li-ion battery bridging the meso- and microscopic length scales. Rather than attempt to modify existing theory, the present study seeks to contribute with a series of observations related to a realistic charge/discharge rate. It is the hope that this work helps to link the bulk-scale measurements and micro-/nano-scale observations, by revealing the microstructural changes occurring as a function of "standard" operation of a commercial Li-ion battery, as may be encountered in consumer applications.

Within the scope of the present study, the following hypotheses have been formulated:

1. X-ray microscopy is a viable technique for non-destructively observing the interiors of commercial batteries.
2. Changes within the microstructures of Panasonic NCR-18650Bs will be observed as a function of aging.

The present experiment has been designed with the primary objective of developing a workflow for image-based characterization of commercial 18650 batteries as a function of electrochemical aging. Thus, the hypotheses above will be evaluated with this primary objective in mind, using the cycling behavior of a specific cell chemistry as the case study. While a thorough characterization is beyond the scope of the present experiments, the present study represents the first of its type known to the author in developing this research framework. It is thus a limitation of this study that the experiments will not be carried out with a high degree of experimental rigor; instead, the study will focus on the method development and leave the rigorous investigation for future research.

CHAPTER FOUR
MATERIALS & METHODS

4.1 Materials

In the present study, a single-cell secondary-type Li-ion battery was used as the model system, formed into the "18650" cylindrical geometry (measuring 18 mm in diameter and 65 mm in length). The batteries used in the study were sourced from a commercial retail outlet, manufactured by Panasonic Corporation, and marketed as the NCR 18650 cells. These batteries have been reported to be constructed of a proprietary "NCA" chemistry, reported elsewhere as incorporating a $LiNi_{0.82}Co_{0.15}Al_{0.03}O_2$ positive electrode [46].

The NCR 18650 cells have been characterized by Panasonic to show a capacity fade of ~30% when charged at 0.5C and discharged at 1C for 400 cycles [47]. For higher discharge C rates, this capacity fade may be expected to increase [47].

4.2 Imaging System

As discussed previously, the X-ray microscopy (XRM) technique has been steadily gaining adoption in recent years, with numerous facilities now available worldwide for access to the equipment. XRM is based on the classic technique of computed tomography (CT), with a rich history in both medical and industrial settings alike.

4.2.1 System Geometry

X-rays are initially produced in a sealed-tube source, where a current passing through a filament at a fixed accelerating voltage creates a beam of electrons that are incident on a target material. Based on interactions between the electron beam and the target material, a spectrum of both characteristic emission energies and *bremsstrahlung*

(broad-band) radiation are produced, unique to each target material and a function of accelerating voltage, as depicted in Figure 12. [48]

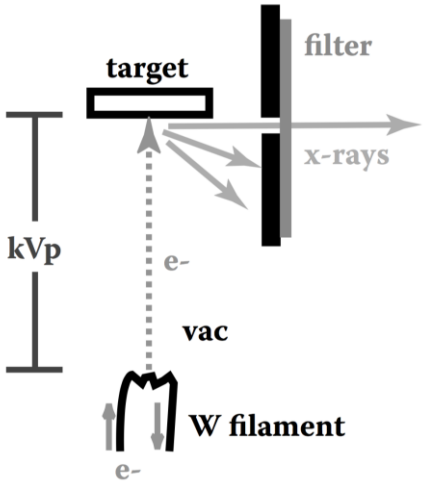

Figure 12. Schematic diagram of X-ray production from a sealed-tube laboratory source. Electrons are accelerated from a filament toward the target material. Based on interactions between the electron beam and the atoms in the target material, X-ray radiation is produced [48]. Republished with permission of Tayler & Francis, from Microcomputed tomography: methodology and applications by Stock, Stuart R., 2009; permission conveyed through Copyright Clearance Center, Inc.

As the X-rays leave the tube source, they are projected with a conical profile through the specimen material, where they interact with the material, attenuating the amplitude of the signal depending on the interactions with specific components within the specimen. The resulting X-ray beam then reaches an X-ray sensitive detector, where the signal is recorded on the basis of amplitude. By collecting several such projection X-ray radiographs at different specimen angles (as shown in Figure 13), a series of radiographs are produced containing 3D volumetric information about the specimen. [48]

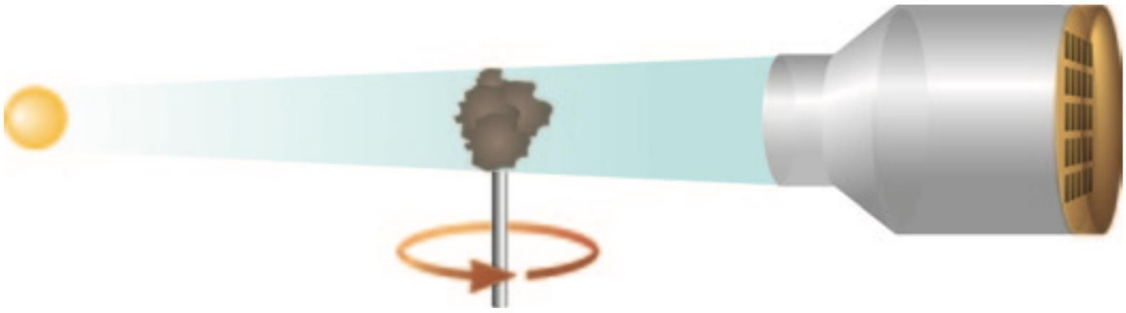

Figure 13. In the XRM setup, projection X-ray radiographs are collected at various specimen rotation angles, with magnification primarily achieved by the detector [22]. Reprinted with permission of Cambridge University Press.

By processing this *tomography* data stack with a computational algorithm (such as Feldcamp-Davis-Kress, or *FDK*) in the Zeiss XMReconstructor software, a 3D stack of tomograms is produced, containing volumetric "virtual slice" data about the specimen's interior [48]. While Figure 14 shows a schematic of the reconstruction technique, a complete description is beyond the scope of this report and the reader is, instead, referred to the references for more information (e.g., [48-51]).

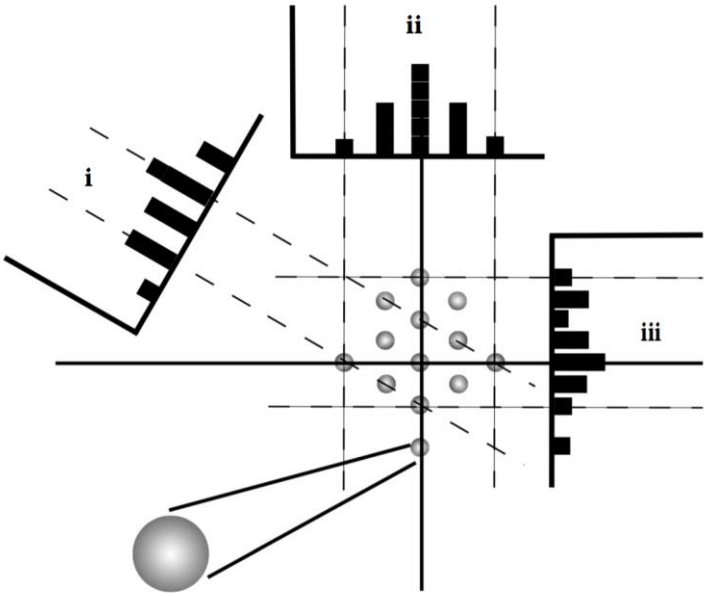

Figure 14. In tomographic reconstruction techniques, the imaging information from each angle is combined with the information from the other angles to virtually "reconstruct" a 3D model of the specimen interior [48]. Republished with permission of Tayler & Francis, from Microcomputed tomography: methodology and applications by Stock, Stuart R., 2009; permission conveyed through Copyright Clearance Center, Inc.

4.2.2 Imaging Apparatus

In the present experiments, a Zeiss Xradia 520 Versa X-ray microscope was used for the non-destructive 3D imaging. This particular XRM system uses a scintillator coupled to an optical objective in the detection system (a 16-bit charge-couple device detector), which provides the unique capability to capture high-resolution data within larger specimens. This particular advantage is especially beneficial for imaging 18650 battery specimens, owing to the typically large size of the commercial batteries and small size of the internal features of interest. Figure 15 shows a battery installed in a Zeiss Xradia Versa XRM system for reference.

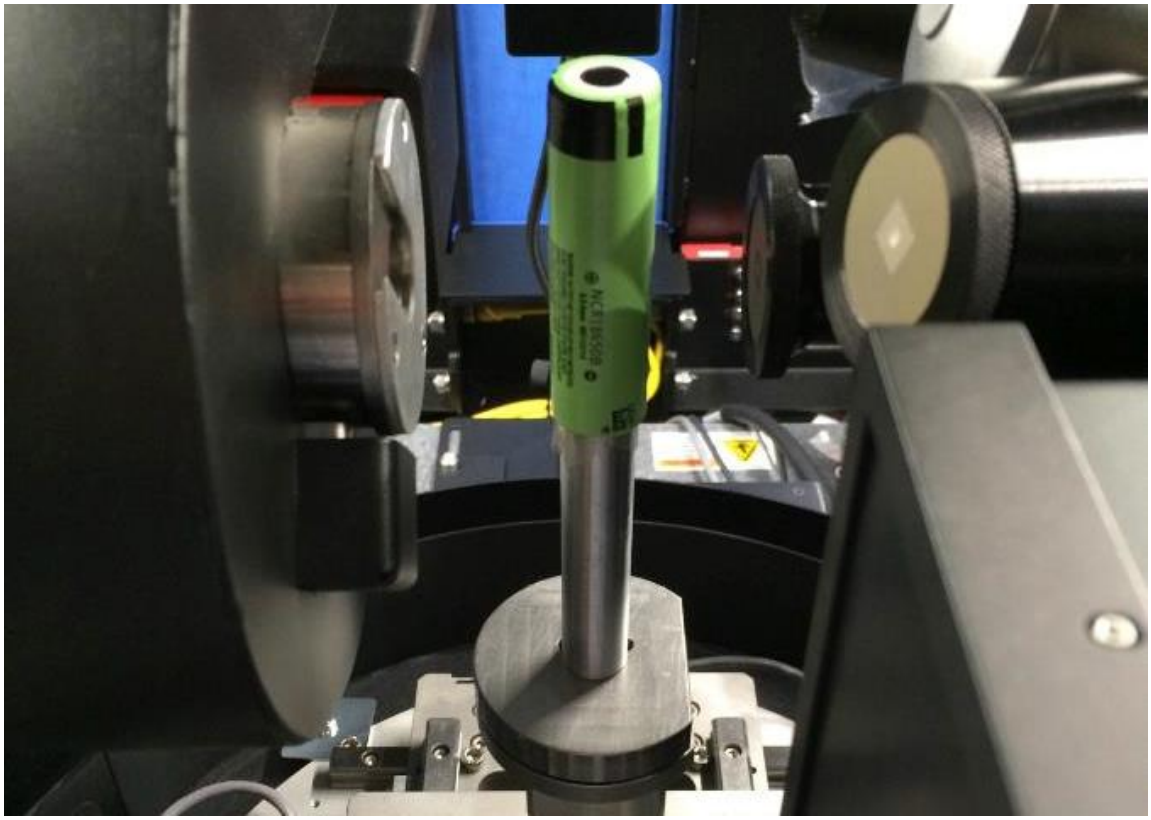

Figure 15. Photo of a Panasonic NCR 18650 Li-ion cell inside the Xradia Versa.

4.3 Data Analysis

After reconstruction, the 3D data were loaded into Visual Si Advanced by Object Research Systems, a data analysis package designed for processing 3D XRM data. This software allows datasets to be explored in 3D, affording fast access to specimen interior information in a dynamic interaction environment. One unique feature of this software is the ability to draw arbitrary "paths" through the 3D volume and "straighten" those paths into a single virtual slice representation. In the case of cylindrical (i.e., nonlinear) battery microstructures, this capability allows the user to virtually unroll the active materials to visualize the planar microstructures.

4.4 Charge Cycling Apparatus

The battery specimens were charge cycled using a Maccor multichannel testing device, connected to a PC for control over the cycling, shown in Figure 16. In parallel with cycling the batteries, the apparatus also recorded voltage as a function of current capacity, enabling the capacity fade to be measured as a function of the increased number of charge cycles.

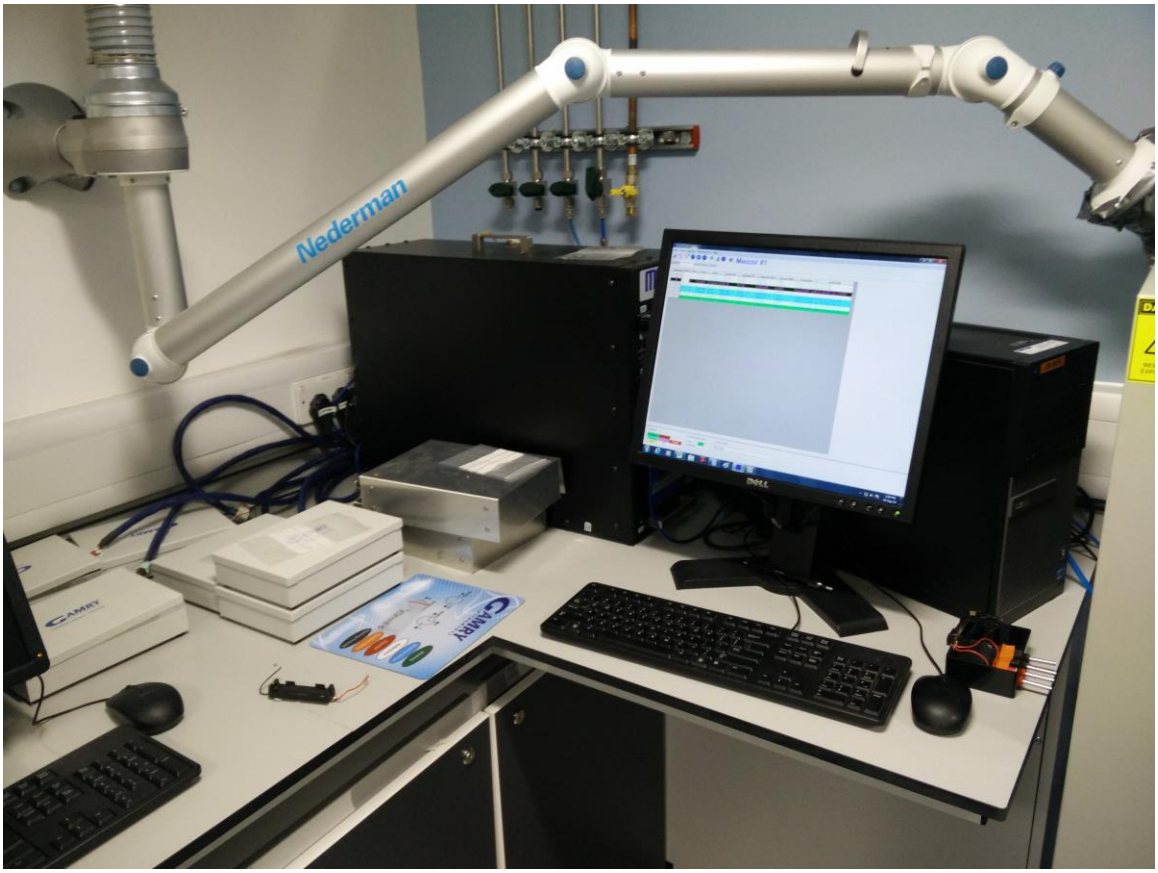

Figure 16. Photo of the Maccor charge cycling apparatus, connected to a PC for control and measurement.

4.5 Experimental Procedure

A single battery was imaged in 3D using the XRM system described above in its "pristine" state – that is, as received from the manufacturer – and then subjected to

increasing numbers of charge cycles. The battery was cycled at a rate of "1.5C," or a 40 minute charge and 40 minute discharge cycle, and then imaged again using the same exposure parameters once a noticeable capacity fade had been observed. This procedure was subsequently repeated for two more batteries, in order to increase the statistical confidence in the results. Three more batteries were imaged in their pristine state and then imaged again without undergoing any aging routines, while traveling from the USA lab to the UK alongside the experimental group – the purpose of those batteries was to serve as a "control group," in order to isolate the electrochemically-induced aging from simple temporal aging.

When all 3D data was collected, the datasets were loaded into Visual Si Advanced for segmentation and data analysis. The before/after paired datasets were aligned to each other and the cathode layers virtually "unrolled" in order to examine the microstructural changes in a planar geometry. Comparing the fresh to the aged state ("experimental group") revealed any changes in microstructure occurring as a result of aging, while comparing the fresh to transported batteries helped to indicate the accuracy of the measurements.

4.6 Imaging Procedure

4.6.1 Sample Preparation and Mounting for XRM

The 18650 cells were mounted on a custom-designed post with the top caps facing up, fixed at the bottom with double-sided tape and secured on their sides with single-sided tape. An alignment mark was drawn on the sample holder and the outer casing of the battery, which indicated the rotational alignment to be used when imaging the cells

after transport / aging. The same mount was used with the same cell in all scans, in order to ensure consistency of alignment. Figure 17 shows a photo of one 18650 as mounted for XRM imaging.

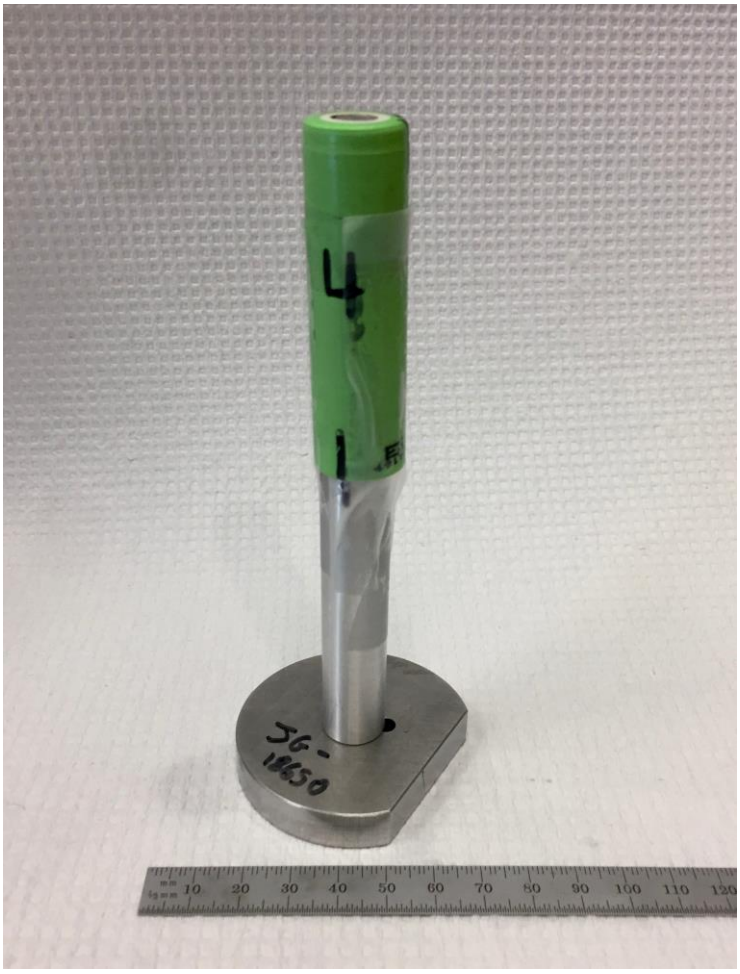

Figure 17. Photo of one 18650 as mounted on the sample holder. An alignment mark drawn on the cell and the holder assisted in the rotational alignment when the batteries were removed from the holder and replaced after aging.

4.6.2 Imaging Location and 4D Specimen Registration

One of the challenges in a 4D imaging study where the specimen must be removed from the holder lies in the re-registration of the specimen when it is replaced in the holder. In order to ensure consistency in the ROI, a specific imaging procedure was

developed to easily return to the same position, using 2D X-ray radiographs at 0° and 90° rotational positions. The procedure began with centering the top of the central pin, as shown in Figure 18, using a pixel size of ~15 µm (X-ray source positioned 21 mm from the rotation axis and detector 72 mm from the rotation axis, using a 0.4X objective lens and factor of 2 detector downsampling). The specimen was then moved up into the X-ray beam by 32.50 mm, to center the 65 mm long battery in the microscope's field of view, as shown in Figure 19. Finally, as shown in Figure 20, the specimen was offset by 3.20 mm in the +X direction and 2.50 mm in the -Z direction, to ensure that the 3D imaging volume was filled with layers of the wrapped electrode foils.

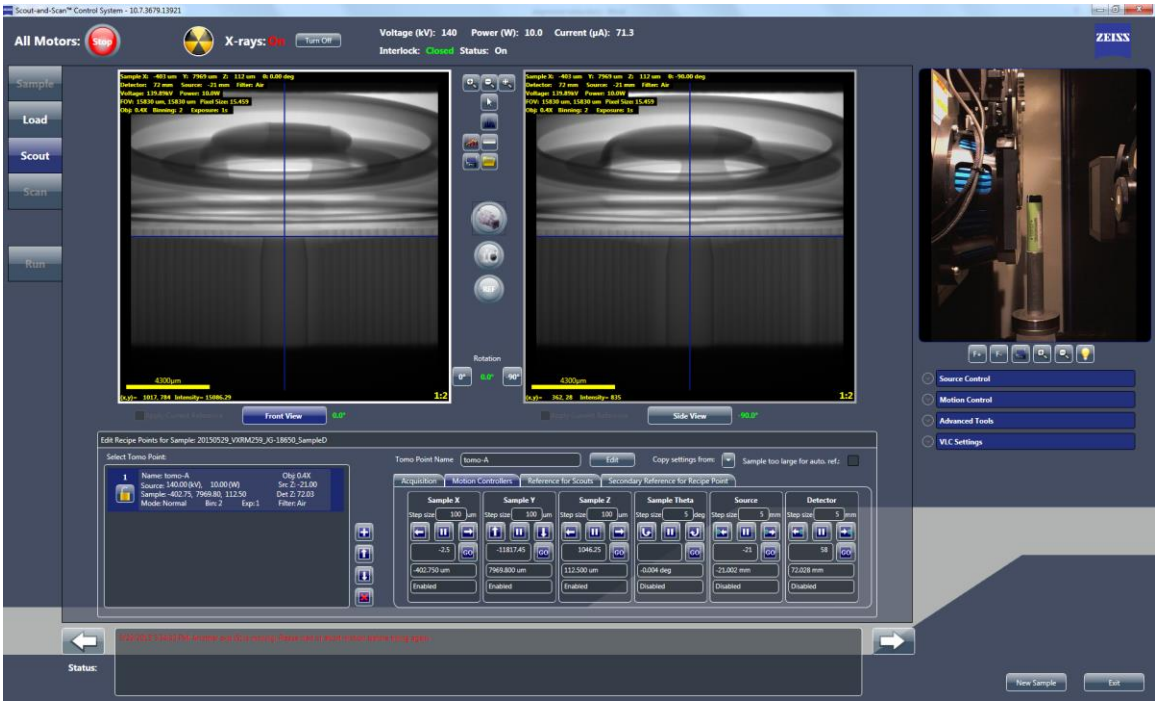

Figure 18. The first step in the specimen alignment procedure was to center the top of the central pin onto the rotation axis.

Figure 19. Moving the specimen upwards in the X-ray beam to center the specimen in the XRM's field of view.

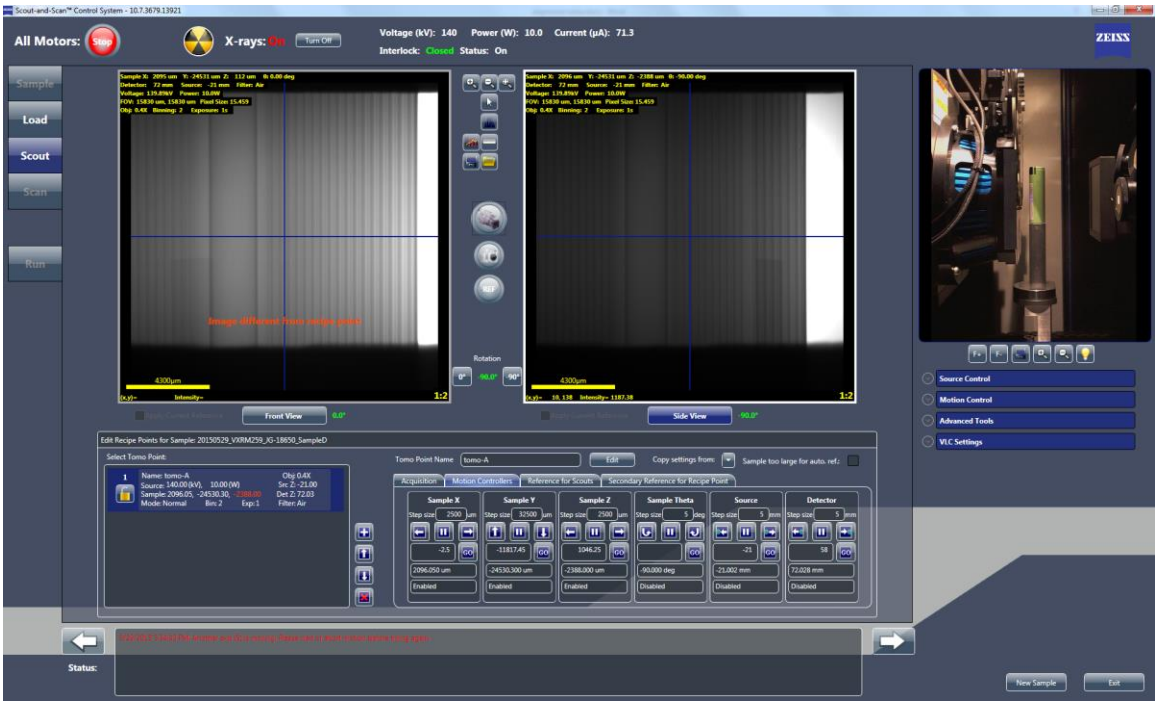

Figure 20. The specimen was offset in the X and Z directions to capture a high-resolution field of view containing many electrode layers.

4.6.3 Imaging Parameters

In all cases, two scans were collected: the first was a "full field of view" (FFOV) scan, which covered the entire specimen, while the second was a "high resolution" (HiRes) interior tomography.

For the FFOV scans, the source was set to 21 mm from the rotation axis and the detector to 72 mm from the rotation axis. A 0.4X objective lens provided image demagnification on the detector, producing a voxel size of 22 µm. 1601 radiographs were collected over a 360° rotation angle range, exposing for 1 second per projection image at a detector downsampling factor of 2. The total exposure time for each FFOV scan was ~1.5 hours, including overhead.

In the HiRes scans, the source was set to 23 mm from the rotation axis and the detector to 62 mm. For the increased resolution, a 4X objective lens was used to provide a voxel size of 1.8 µm using a detector downsampling factor of 2. The interior tomography required a larger number of projection radiographs to suppress imaging artifacts [52], thus 5001 views were collected at an exposure time of 10 seconds per view over a 360° rotation angle range. The total time for each HiRes scan was ~15 hours, including overhead.

4.7 Equipment Access

The charge cycling apparatus was located in the Electrochemical Innovation Laboratory at University College London in London, UK [53], where the cycling studies were performed. Specimens were transported to and from the facility using express parcel delivery, to minimize the damage due to handling. Imaging studies were

performed at the Carl Zeiss X-Ray Microscopy headquarters in Pleasanton, CA, USA, where an Xradia 520 Versa was available for the experiments.

4.8 Safety

4.8.1 Li-ion Battery Handling

The combined use of Li-ion batteries and X-ray imaging instrumentation in the present required some awareness of potential safety issues in the experimental methods. From the documentation provided by the Li-ion battery manufacturer, several procedural guidelines were followed in the charge/discharge process [54]. The "constant voltage/constant current" mode was used, taking care to install the batteries with correct polarity [54]. The single batteries were charged up to 4.2 V at room temperature (suggested temperature range: 10°C to 45°C), and discharged down to 3.0 V at room temperature (suggested temperature range: -10°C to +65°C) [54]. Before performing any charge/discharge cycles or before handling, the batteries were inspected for structural integrity and signs of casing damage, puncture, electrolyte leakage, or abnormally high temperature [54].

4.8.2 X-Ray Safety

The x-ray microscopes used in the present study work based on ionizing radiation, which has the potential to pose some additional safety hazards. These X-ray systems are insulated from leakage and most safety precautions are already taken by the manufacturer. Some potential safety risks, such as those related to high-voltage electrical shock and radiation leakage, were significantly reduced by ensuring that the redundant interlock system was enabled [55]. Other potential safety risks, such as magnetic fields,

low-voltage electrical shock, and pinch hazards, were minimized through mindful operation of the equipment [55]. The system is reported to contain lead (as shielding in the enclosure) and thallium-doped cesium iodide (in the detection system), but both of these materials are not exposed to the user so the hazard risk was negligible [55]. Leakage rates of ionizing radiation during typical operation is reported by the manufacturer as <<1 μS/hr, which was confirmed via pre-operation survey with a calibrated Geiger counter [55]. In the event of any emergency situation, the system was equipped with an emergency off (EMO) button, which would remove power to the system and immediately shut down both the X-ray source and the motion controller [55].

4.8.3 Cycling Test Safety

In the Maccor battery testing apparatus, all cycling tests were performed inside a Faraday cage with a Nederman extraction arm above the device, to protect the operators in the event of gas venting. The batteries were observed for the first several hours to ensure that no problems were occurring, then were monitored periodically during the cycling tests. A full disclosure regarding safety protocols was submitted to the UCL laboratory facility manager, outlining the safety risks and mitigation protocol outlined here.

CHAPTER FIVE
RESULTS & DISCUSSION

5.1 Cycle-Testing Results

The cycling rate of 1.5C was found to produce a rapid cell degradation, which led to a substantial capacity fade in all three experimental cells. In two cases, the cells failed, and in all three cases the capacity fade was consistently on the order of ~20%.

Figure 21 shows the voltage vs. capacity curves for all three batteries in the experimental group, while Figure 22 shows the capacity vs. cycle number for the same three batteries. In the voltage vs. capacity curve, both an upswing (positive slope) and downswing (negative slope) were observed, representing the charge and discharge behaviors, respectively. These plots indicate a change in battery performance as the batteries age, which is manifested as a drop in maximum current capacity (see Figure 22).

As evidenced by Figure 22, the maximum current capacity changes from the specified value of ~3.2 Ah [47] to a value of ~2.5 Ah when the batteries were removed from the cycling apparatus. This represents a ~20% maximum current capacity fade as a result of the aging routine, leading to ultimate failure of the batteries after 35 cycles in the case of Sample #2 and 37 cycles in the case of Sample #3. In the case of Sample #4, the battery did not fail, but was removed from the cycling apparatus after the capacity had faded to a similar value as the other two batteries: namely, after 55 cycles. This was done to introduce electrochemical consistency in the results, in order to achieve similar conditions for the imaging investigation. It is interesting to note that the aging responses of Sample #2 and Sample #3 were consistent with each other, while the response of Sample #4 was considerably more stable over time (in terms of maximum current

capacity). The reasons for this remain unknown, though it may point toward some intrinsic variability in the aging behavior of these particular commercial batteries.

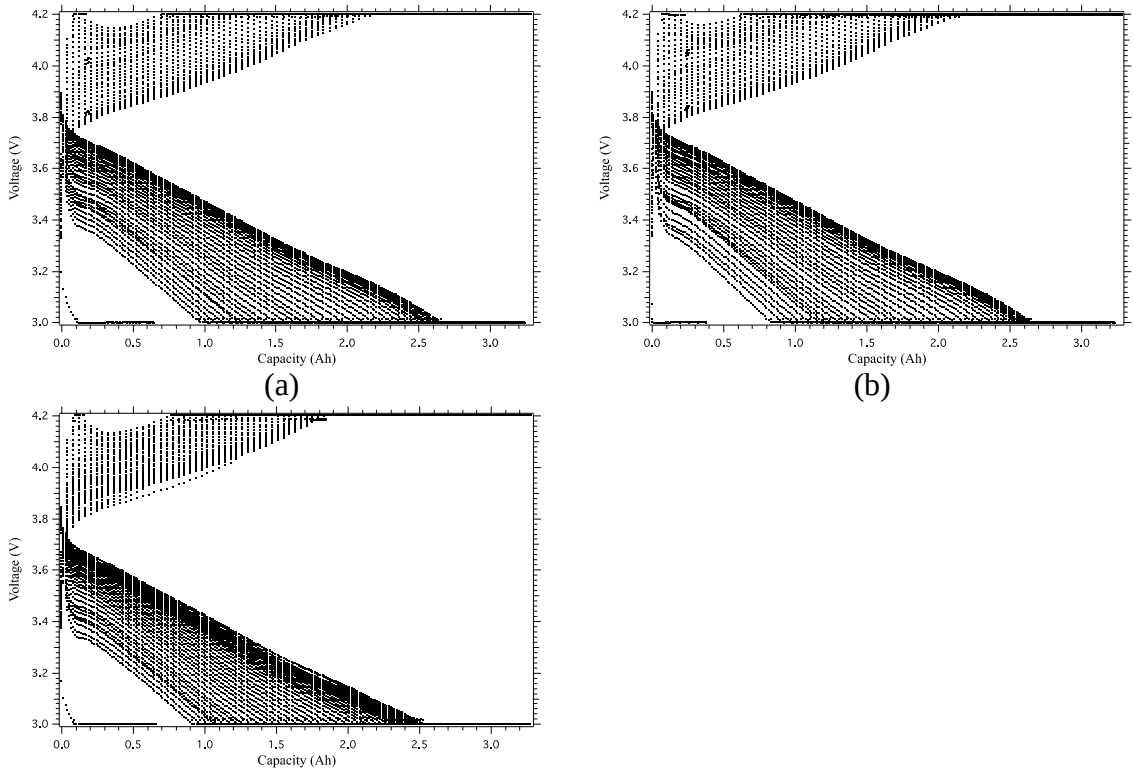

Figure 21. Voltage vs. capacity curves for each battery in the experimental group. (a) Sample #2, (b) Sample #3, (c) Sample #4. The positively sloped portion of the plots corresponds to charging characteristics, while the negatively sloped portion corresponds to discharge behaviors.

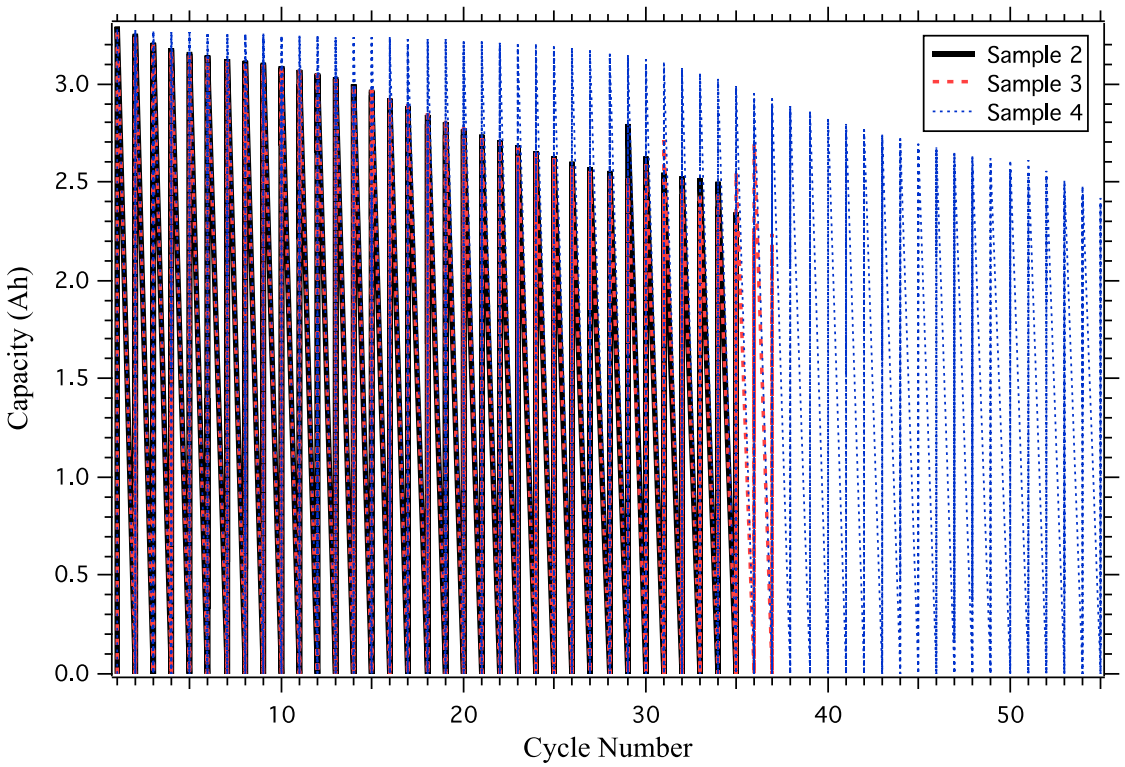

Figure 22. Capacity vs. cycle number for all three batteries in the experimental group. Sample #4 did not fail, but was removed from the cycling apparatus when the capacity fade was consistent with the other three batteries.

5.2 Imaging Results

5.2.1 ROI Alignment and Dataset Registration

As previously outlined, the same battery cells were imaged before and after the cycling experiments, and care was taken to ensure that the same regions of interest (ROIs) were examined in each case. Despite the best efforts to achieve consistent positioning, slight offsets in the specimen rotation on the sample holder and spatial [re-]localization of the ROI yielded slightly different imaging volumes in the XRM. To account for this, bright inclusions in the 3D volumes were used as registration points,

typically using 2-3 such points per dataset. From these registrations, then, it could be assured that the same regions were captured by the XRM in both the fresh and aged states. An example of this alignment is shown in Figure 23.

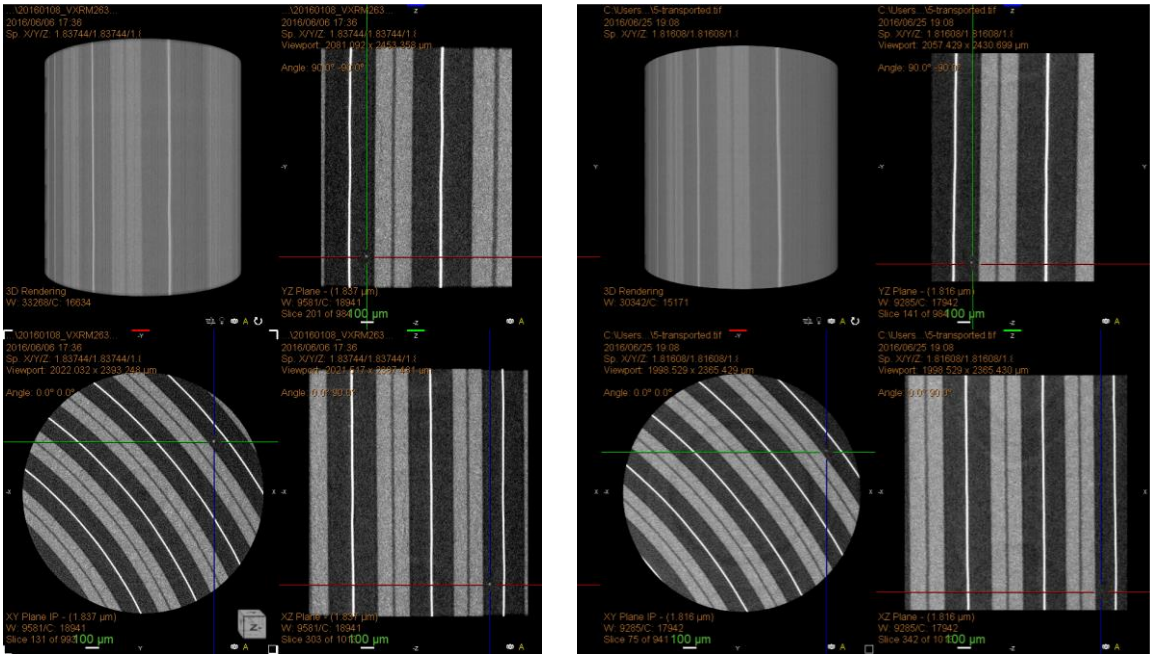

(a) (b)

Figure 23. Bright inclusions within the data volumes were used for 3D registration of the (a) fresh and (b) aged results. The position of the crosshairs indicates the position of one such bright inclusion used for registration on an example dataset.

5.2.2 Data Analysis Procedure

With the results aligned to each other, a path was drawn on each image across the same position within each specimen, taking care to adjust the length and position of the path to account for the offset in dataset alignments. One such path is shown in Figure 24. These paths were then virtually straightened, to show the microstructure of the specimen in a planar view, in spite of the curved nature of the actual specimen. This procedure was performed on the set of 3 batteries in the experimental group, as well as in the set of 3

batteries in the control group. The data analysis method employed is a unique capability of the analysis software and the present study represents the first application of this technique known to the author at the time of this writing.

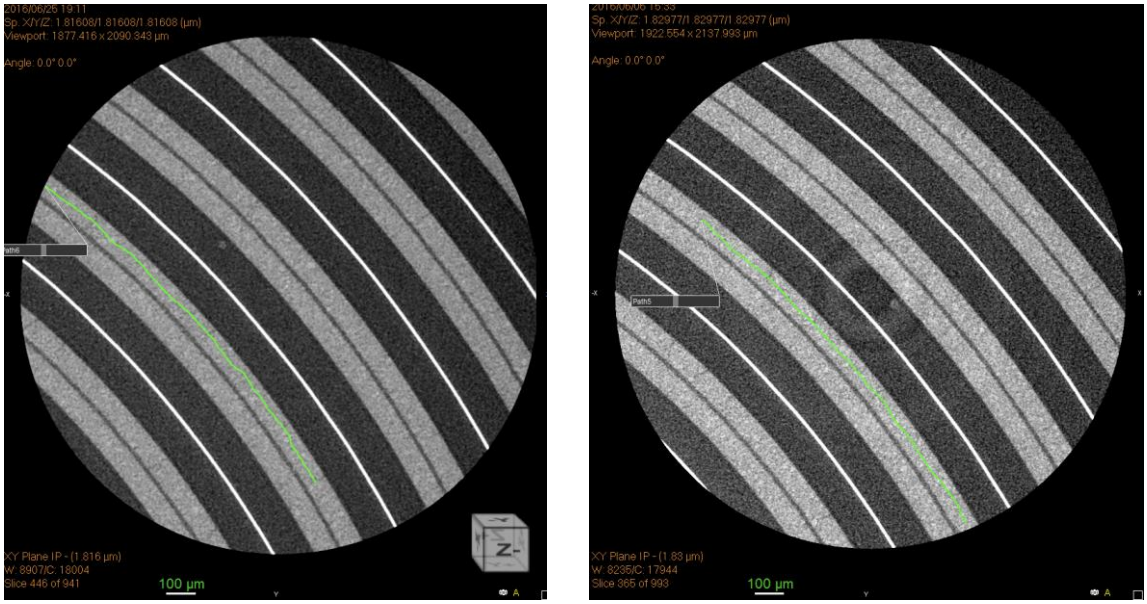

(a) (b)

Figure 24. A path (highlighted in green) was drawn through the aligned 3D datasets, accounting for the offsets between the (a) fresh and (b) cycled states. This path identified the region for virtually unrolling the battery to reveal the planar microstructure of the curved section.

5.2.3 High-Resolution X-Ray Micrographs

The X-ray micrographs from this study were used to non-destructively observe the layers of active materials within the batteries in both the fresh and aged states. These micrographs are virtually unrolled sections, following the procedure outlined previously, and reveal some changes between the fresh and aged microstructures in the experimental group, as well as fewer changes in the control group. Figure 25 shows the X-ray

micrographs from the experimental group (before/after transport and aging), while Figure 26 shows the X-ray micrographs from the control group (before/after transport only).

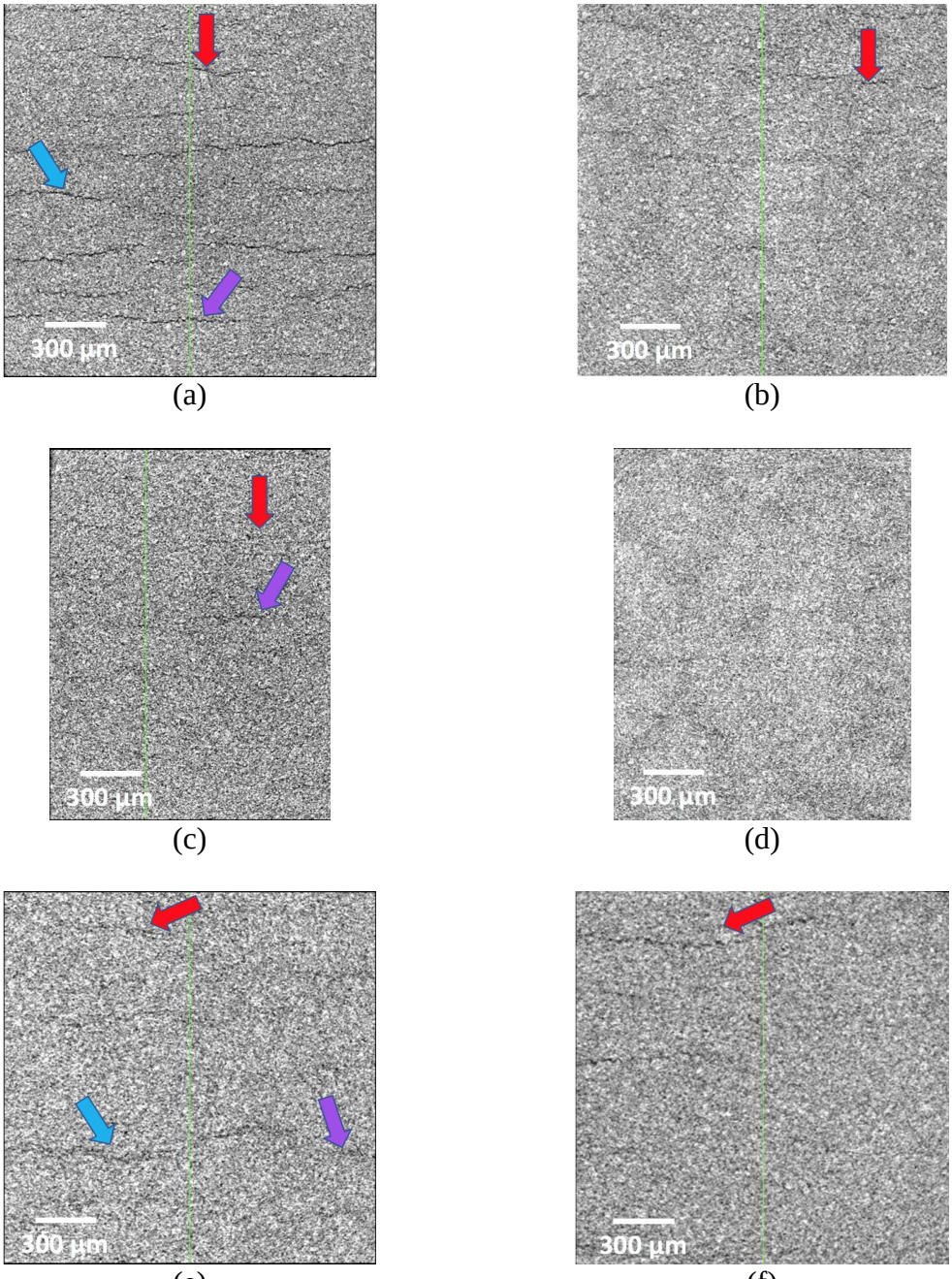

Figure 25. X-ray micrographs from the virtually straightened sections of the experimental group batteries taken at the same position within the cells. (a) shows the first cell in its fresh state, (b) the first cell in its aged state, (c) the second cell in its fresh state, (d) the second cell in its aged state, (e) the third cell in its fresh state, and (f) the third cell in its aged state. The colored arrows indicate observed cracks in the microstructure.

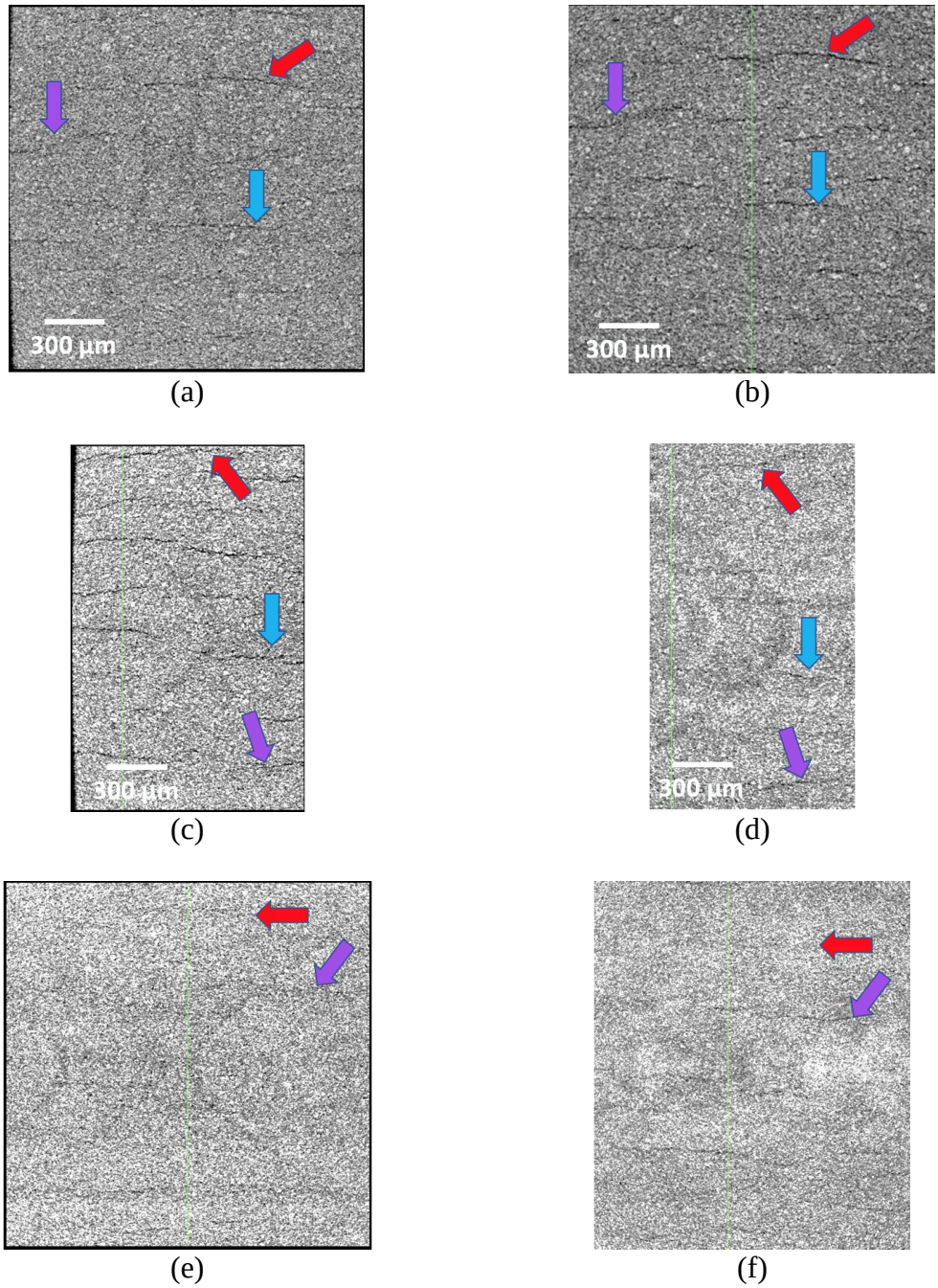

Figure 26. X-ray micrographs from the virtually straightened sections of the control group batteries taken at the same position within the cells. (a) shows the first cell in its fresh state, (b) the first cell after transport, (c) the second cell in its fresh state, (d) the second cell after transport, (e) the third cell in its fresh state, and (f) the third cell after transport. The colored arrows indicate observed cracks in the microstructure.

5.2.4 Interpretation and Discussion

Based on examining the experimental group results, there is a systematic change observed within the specimens after transport and aging. In all three cases, many cracks are observed in the fresh cells, which are not observed in the aged cells. This result indicates that cracks within the batteries may reduce or even disappear after cycling, leading to different microstructures once the cells have been in service. The comparison in the control group exhibits substantially less change than that observed in the experimental group, with many cracks existing in the fresh state still observed in the transported state. Thus, the results of this study indicate that aging (i.e., electrochemical operation) plus transport is more strongly related to microstructural change than transport alone, pointing toward service as a potential cause of the change.

Possible reasons for the cracks disappearing after aging remains an interesting topic for both speculation and future research. The present study represents the first of its kind that attempts to systematically – and non-destructively – observe changes in the interior microstructure of an 18650 under demanding aging conditions. It is conceivable that even pristine electrode foils may crack when they are rolled and packed, due to the mechanical stresses imparted by the rolling process, so the observation of cracks in the commercially packaged cells may not be surprising. When in operation, the electrode particles expand and contract as lithium ions enter and exit the particle matrices, which may cause the particles to migrate in order to relieve the newly-formed anisotropic stress gradients and achieve mechanical equilibrium.

The motion of particles upon lithiation/delithiation may cause any cracks in the original structure to disappear in response to the particle migration. In response, the pore networks and fluid transport pathways within the cell would consequently change, and there may even be nano-scale breakage of the particle-particle bonds if the binder adhesion between particles is too small to resist the migratory stress. In essence, the smaller features of the microstructure may exhibit significant changes in response to the cycling processes, which were only observable at this length scale in terms of micron-scale crack disappearance. Further work should be performed at the nano-scale to observe the actual effects of cycling behavior on the smaller details of the battery electrode microstructure evolution in order to better understand the reasons for the observations from the present study.

5.3 Cell Failure Investigation

One remaining curiosity from the results of the aging experiments lies in the reasons for the cell failures. From the manufacturer's specifications, the recommended operating temperatures of the batteries range from 0°C to +45°C during charge and -20°C to +60°C during discharge [47]. The temperatures of the cells were monitored during the aging experiments and an excerpt from those results is shown in Figure 27. These temperature measurements indicate that the batteries were routinely exceeding temperatures of 50°C, which is nearly the maximum specified operating temperature. For this reason, thermal overload was suspected as being a key contributor to the premature cell failure.

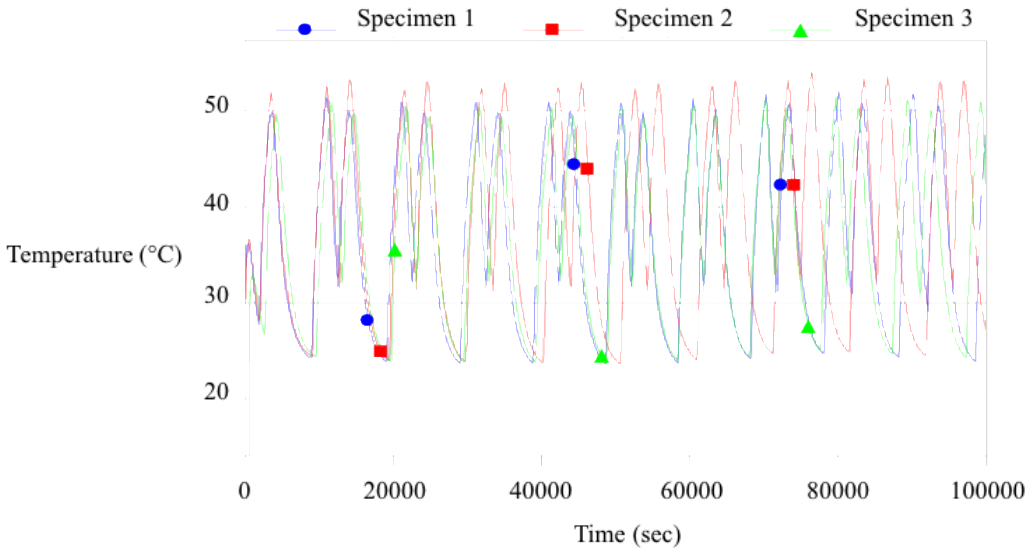

Figure 27. Thermal behavior of the batteries during the cyclic aging routine. The temperatures routinely reached over 50°C, pushing the upper limit of the recommended operating temperatures based on the manufacturer's specifications.

A typical 18650 battery cell contains a complex assembly within its top cap, which includes protections against high temperatures (to avoid thermal runaway and associated consumer safety risks). The thermal protection is typically achieved with a current interrupt device (CID), as illustrated in Figure 28, which acts as an electronic switch that changes shape and disconnects the battery if the temperatures exceed a specified range [56]. The CID is a clear indicator of thermal overload; thus, by observing its shape, one can clearly identify whether or not the battery's failure was related to exceptionally high temperatures.

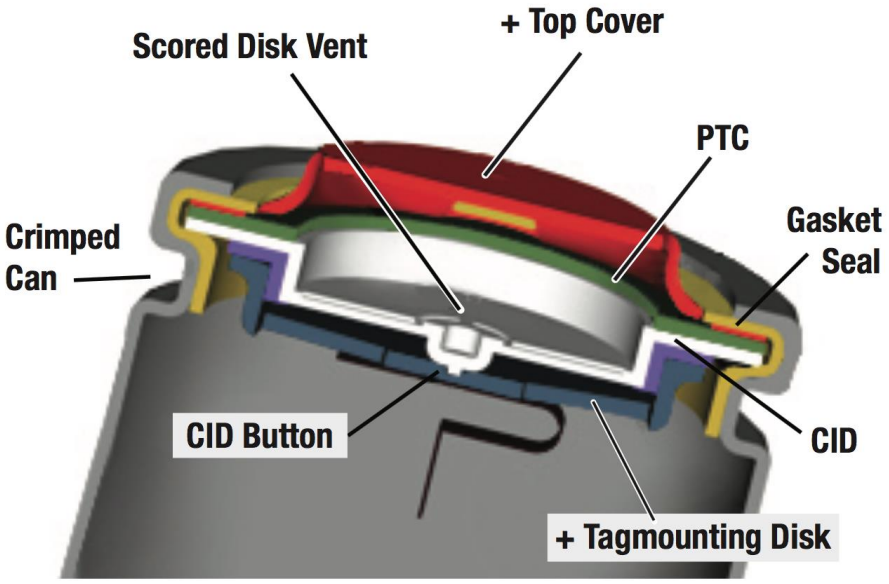

Figure 28. Schematic of a typical Li-ion battery top cap, showing the CID shaded in white [56]. Credit: NASA. Reprinted with permission.

In the XRM scans, a low-resolution image was collected as part of the imaging routine, in order to check for large-scale changes. While the top cap was not specifically imaged during the routine, it was nevertheless possible to collect an image of the top cap on a failed battery and an image of the same ROI on a fresh battery to compare the geometry of the CID. The results of this comparison, performed with 22 μm voxel size, are shown in Figure 29.

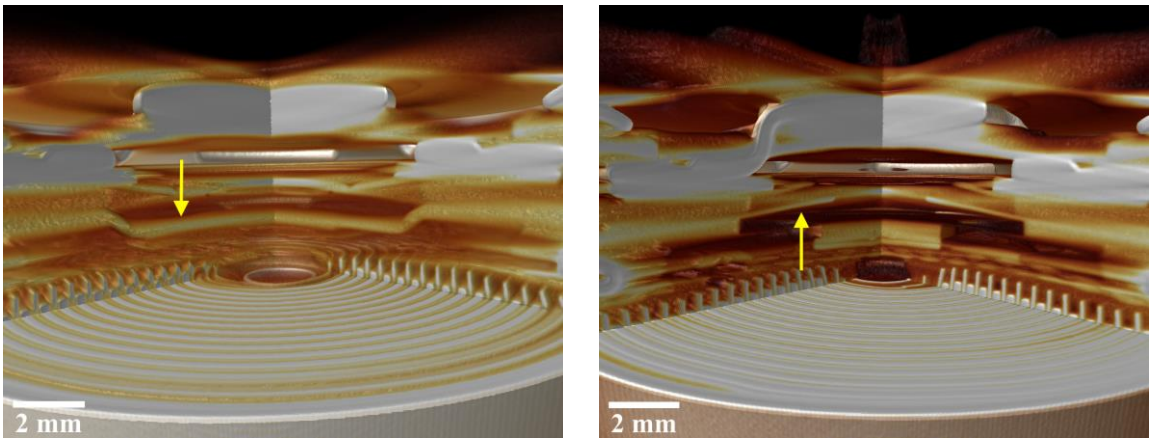

(a) (b)

Figure 29. Comparison 3D X-ray micrographs of the top cap interiors in the (a) fresh and (b) aged (failed) batteries. The yellow arrows indicate the position of the CID within the top cap assembly, clearly showing a shape/direction change between the two states.

From the 3D cutaway renderings, a shape change in the CID is clearly observed. In the case of the aged (failed) battery, a disconnection between the CID and the CID button may be seen, which would be expected to cause a failure of the device (by engaging the thermal protection apparatus). Thus, it was concluded that thermal overload was a possible cause of the ultimate cell failure, which indicates that thermal management solutions should be put into place when the cells under study are subjected to high cycling rates.

CHAPTER SIX
CONCLUSIONS & FUTURE WORK

As previously mentioned, the primary purpose of this work was to assess the viability of using 4D X-ray microscopy (XRM) as a non-destructive imaging technique to characterize the microstructural evolution of commercially-packaged Li-ion batteries after aging. To this end, the experiment successfully demonstrated that, indeed, XRM is well suited for this type of investigation, as it revealed the reduction of cracks in a set of three Panasonic NCR-18650 batteries exposed to aging conditions, which were not as readily observed in the same batteries that were not subjected to aging conditions. It was determined that the charge/discharge rates were sufficiently high to introduce thermal changes, which caused the current interrupt device (CID) to engage, resulting in cell failure. In future work, researchers may build on these results, using the XRM technique to study different aspects of the microstructure evolution, either on similar batteries or applied to different geometries (e.g., pouch or prismatic cells). Pouch cell geometries may be of especial interest, as the polymer packages should facilitate X-ray transmission and increase the quality of the X-ray micrographs for a volumetric microstructure analysis.

Future researchers may, thus, focus their efforts on examining the mechanisms of cell degradation, such as thermally-induced changes (e.g., extreme high or low temperatures), or pressure-induced changes (e.g., simulating impact in an automotive application). Given that thermal overload was determined to be one cause of ultimate cell failure in the present experiments, future studies should isolate (or eliminate) the thermal effects, via thermally-induced microstructure evolution analysis or integrating

thermal management systems (e.g., cooling jackets). Slower charge/discharge rates may also be helpful in reducing the thermal load on the battery. It may also be of interest to expand the technique to incorporate other imaging modalities (such as high-resolution optical microscopy, nano-scale X-ray microscopy, or scanning electron microscopy) to probe the multi-scale nature of the microstructure evolution. Furthermore, by coupling the imaging results with digital modeling or computational simulation approaches, it may be of interest to examine how the batteries may be expected to degrade, and use the XRM approach to validate / refine the models of cell evolution.

Finally, future work may seek to reduce the noise and/or imaging artifacts in the XRM results. This may be achieved through using prolonged image acquisition times, or, as previously mentioned, by changing the cell form factor to one that is more conducive to X-ray transmission. The present study represented one preliminary workflow, but there may be opportunities to improve the results via additional process development in imaging parameters specific to each cell geometry.

The present study represents the first of its kind, in which a workflow was developed for image-based analysis of Li-ion battery microstructure evolution. The material system chosen was particularly challenging, given the complexity of the evolution processes and abundance of unknowns in the experiment. Nevertheless, a research framework was established that may be readily applied to other battery systems or different electrochemical or environmental stimuli. The results, thus, provide a valuable baseline contribution for future battery imaging studies within a variety of contexts.

REFERENCES

1. D. Linden and T.B. Reddy, Handbook of Batteries, (McGraw-Hill Professional. 2002).

2. Mitsubishi, *"Developing Batteries for EVs and Future Societies,"* http://www.mitsubishicorp.com/jp/en/mclibrary/business/vol1/ (accessed August 29, 2015).

3. A. Mirza, *"GE Watt Station a Technology Assessment,"* https://stonybrook.digication.com/abbasmirza/GE_Watt_Station_a_Technology_Assessment (accessed August 29, 2015).

4. *"Global EV Outlook,"* https://www.iea.org/publications/globalevoutlook_2013.pdf (accessed September 6, 2015).

5. M. Ebner, F. Marone, M. Stampanoni and V. Wood, "*Visualization and quantification of electrochemical and mechanical degradation in Li ion batteries*," Science. **342** 716–720 (2013).

6. P.R. Shearing, L.E. Howard, P.S. Jørgensen, N.P. Brandon and S.J. Harris, "*Characterization of the 3-dimensional microstructure of a graphite negative electrode from a Li-ion battery*," Electrochemistry Communications. **12** 374–377 (2010).

7. D. Kehrwald, P.R. Shearing, N.P. Brandon, P.K. Sinha and S.J. Harris, "*Local Tortuosity Inhomogeneities in a Lithium Battery Composite Electrode*," J. Electrochem. Soc. **158** A1393–7 (2011).

8. J.M. Tarascon and M. Armand, "*Issues and challenges facing rechargeable lithium batteries*," Nature. (2001).

9. B. Scrosati, B. Scrosati, J. Garche and J. Garche, "*Lithium batteries: Status, prospects and future*," Journal of Power Sources. **195** 2419–2430 (2010).

10. M. Yoshio, R.J. Brodd and A. Kozawa, Lithium-Ion Batteries: Science and Technologies, (Springer. 2009).

11. J. Christensen and J. Newman, "*Stress generation and fracture in lithium insertion materials*," J Solid State Electrochem. **10** 293–319 (2006).

12. X. Zhang, W. Shyy and A. Marie Sastry, "*Numerical Simulation of Intercalation-Induced Stress in Li-Ion Battery Electrode Particles*," J. Electrochem. Soc. **154** A910–7 (2007).

13. K. Zhao, M. Pharr, J.J. Vlassak and Z. Suo, "*Fracture of electrodes in lithium-ion batteries caused by fast charging*," J. Appl. Phys. **108** 073517–7 (2010).

14. W.H. Woodford, Y.-M. Chiang and W.C. Carter, "*"Electrochemical Shock" of Intercalation Electrodes: A Fracture Mechanics Analysis*," J. Electrochem. Soc. **157** A1052–8 (2010).

15. C. Lim, B. Yan, L. Yin and L. Zhu, "*Simulation of diffusion-induced stress using reconstructed electrodes particle structures generated by micro/nano-CT*," Electrochimica Acta. **75** 279–287 (2012).

16. R. Panat, "*A model for crack initiation in the Li-ion battery electrodes*," Thin Solid Films. (2015).

17. K. Takahashi and V. Srinivasan, "*Examination of Graphite Particle Cracking as a Failure Mode in Lithium-Ion Batteries: A Model-Experimental Study*," J. Electrochem. Soc. **162** A635–A645 (2015).

18. H.B. Chew, B. Hou, X. Wang and S. Xia, "*Cracking mechanisms in lithiated silicon thin film electrodes*," International Journal of Solids and Structures. **51** 4176–4187 (2014).

19. S.-C. Chao, Y.-F. Song, C.-C. Wang, H.-S. Sheu, H.-C. Wu and N.-L. Wu, "*Study on Microstructural Deformation of Working Sn and SnSb Anode Particles for Li-Ion Batteries by in Situ Transmission X-ray Microscopy*," J. Phys. Chem. C. **115** 22040–22047 (2011).

20. S.-C. Chao, Y.-C. Yen, Y.-F. Song, H.-S. Sheu, H.-C. Wu and N.-L. Wu, "*In Situ Transmission X-ray Microscopy Study on Working SnO Anode Particle of Li-Ion Batteries*," J. Electrochem. Soc. **158** A1335–5 (2011).

21. S.-C. Chao, Y.-C. Yen, Y.-F. Song, Y.-M. Chen, H.-C. Wu and N.-L. Wu, "*A study on the interior microstructures of working Sn particle electrode of Li-ion batteries by in situ X-ray transmission microscopy*," Electrochemistry Communications. **12** 234–237 (2010).

22. A.P. Merkle and J. Gelb, "*The Ascent of 3D X-ray Microscopy in the Laboratory*," Micros. Today. **21** 10–15 (2013).

23. M. Feser, J. Gelb, H. Chang, H. Cui, F. Duewer, S.H. Lau, et al., "*Sub-micron resolution CT for failure analysis and process development*," Meas. Sci. Technol. **19** 094001–8 (2008).

24. J. Kirz and C. Jacobsen, "*The history and future of x-ray microscopy*," J. Phys.: Conf. Ser. (2009).

25. P.R. Shearing, N.P. Brandon, J. Gelb, R. Bradley, P.J. Withers, A.J. Marquis, et al., "*Multi Length Scale Microstructural Investigations of a Commercially Available Li-Ion Battery Electrode*," J. Electrochem. Soc. **159** A1023–A1027 (2012).

26. I.V. Thorat, D.E. Stephenson, N.A. Zacharias, K. Zaghib, J.N. Harb and D.R. Wheeler, "*Quantifying tortuosity in porous Li-ion battery materials*," Journal of Power Sources. **188** 592–600 (2009).

27. P.R. Shearing, D.S. Eastwood, R.S. Bradley, J. Gelb, S. Cooper, F. Tariq, et al., "*Exploring electrochemical devices using X-ray microscopy: 3D micro-structure of batteries and fuel cells*," Microscopy and Analysis. 1–4 (2013).

28. B. Yan, C. Lim, L. Yin and L. Zhu, "*Three Dimensional Simulation of Galvanostatic Discharge of LiCoO2 Cathode Based on X-ray Nano-CT Images*," J. Electrochem. Soc. **159** A1604–A1614 (2012).

29. J. Nelson, S. Misra, Y. Yang, A. Jackson, Y. Liu, H. Wang, et al., "*In Operando X-ray Diffraction and Transmission X-ray Microscopy of Lithium Sulfur Batteries*," J. Am. Chem. Soc. **134** 6337–6343 (2012).

30. D.-W. Chung, M. Ebner, D.R. Ely, V. Wood and R.E. Garcia, "*Validity of the Bruggeman relation for porous electrodes*," Modelling Simul. Mater. Sci. Eng. **21** (2013).

31. B. Yan, C. Lim, L. Yin and L. Zhu, "*Simulation of heat generation in a reconstructed LiCoO2 cathode during galvanostatic discharge*," Electrochimica Acta. **100** 171–179 (2013).

32. D.S. Eastwood, R.S. Bradley, F. Tariq, S.J. Cooper, O.O. Taiwo, J. Gelb, et al., "*The application of phase contrast X-ray techniques for imaging Li-ion battery electrodes*," Nuclear Instruments and Methods in Physics. **324** 1–6 (2014).

33. F. Tariq, V. Yufit, M. Kishimoto, P.R. Shearing, S. Menkin, D. Golodnitsky, et al., "*Three-dimensional high resolution X-ray imaging and quantification of lithium ion battery mesocarbon microbead anodes*," Journal of Power Sources. **248** 1014–1020 (2014).

34. P. Trogadas, O.O. Taiwo, T.P. Neville, B. Tjaden, J. Parrondo, S. Yun, et al., "*X-ray micro-tomography as a diagnostic tool for the electrode degradation in vanadium redox flow batteries*," **48** 155–159 (2014).

35. L. Zielke, C. Barchasz, S. Waluś, F. Alloin and J.C. Leprêtre, "*Degradation of Li/S Battery Electrodes On 3D Current Collectors Studied Using X-ray Phase Contrast Tomography*," Sci. Rep. **5** 10921 (2015).

36. S.K. Babu, A.I. Mohamed, J.F. Whitacre and S. Litster, "*Multiple Imaging Mode X-ray Computed Tomography for Distinguishing Active and Inactive Phases in Lithium-Ion Battery Cathodes*," Journal of Power Sources. **283** 1–21 (2015).

37. F. Meirer, J. Cabana, Y. Liu, A. Mehta, J.C. Andrews and P. Pianetta, "*Three-dimensional imaging of chemical phase transformations at the nanoscale with full-field transmission X-ray microscopy*," J Synchrotron Rad. **18** 773–781 (2011).

38. J. Wang, Y.-C.K. Chen-Wiegart and J. Wang, "*In situ chemical mapping of a lithium-ion battery using full-field hard X-ray spectroscopic imaging*," Chem. Commun. **49** 6480–3 (2013).

39. J.N. Weker, N. Liu, S. Misra, J.C. Andrews, Y. Cui and M.F. Toney, "*Insitu nanotomography and operando transmission X-ray microscopy of micron-sized Ge particles*," Energy Environ. Sci. **7** 2771–9 (2014).

40. A. Haibel, I. Manke, A. Melzer and J. Banhart, "*In Situ Microtomographic Monitoring of Discharging Processes in Alkaline Cells*," J. Electrochem. Soc. **157** A387–5 (2010).

41. V. Yufit, P. Shearing, R.W. Hamilton, P.D. Lee, M. Wu and N.P. Brandon, "*Investigation of lithium-ion polymer battery cell failure using X-ray computed tomography*," Electrochemistry Communications. **13** 1–13 (2011).

42. Y.-C.K. Chen-Wiegart, P. Shearing, Q. Yuan, A. Tkachuk and J. Wang, "*3D morphological evolution of Li-ion battery negative electrode LiVO2 during oxidation using X-ray nano-tomography*," Electrochemistry Communications. **21** 58–61 (2012).

43. D.S. Eastwood, V. Yufit, J. Gelb, A. Gu, R.S. Bradley, S.J. Harris, et al., "*Lithiation-Induced Dilation Mapping in a Lithium-Ion Battery Electrode by 3D X-Ray Microscopy and Digital Volume Correlation*," **4** 1–7 (2014).

44. D.P. Finegan, M. Scheel, J.B. Robinson and B. Tjaden, "*In-operando high-speed tomography of lithium-ion batteries during thermal runaway*," Nature. **6** 6924 (2015).

45. S.J. Harris and P. Lu, "*Effects of Inhomogeneities—Nanoscale to Mesoscale—on the Durability of Li-Ion Batteries*," J. Phys. Chem. C. **117** 6481–6492 (2013).

46. T. Hayashi, J. Okada, E. Toda and R. Kuzuo, "*Degradation Mechanism of LiNi0. 82Co0. 15Al0. 03O2 Positive Electrodes of a Lithium-Ion Battery by a Long-Term Cycling Test*," J. Electrochem. Soc. **161** A1007–A1011 (2014).

47. Panasonic, *"Lithium Ion NCR18650B,"* http://na.industrial.panasonic.com/sites/default/pidsa/files/ncr18650b.pdf (accessed November 7, 2015).

48. S.R. Stock, MicroComputed Tomography, (CRC Press. 2008).

49. S.R. Stock, "*Recent advances in X-ray microtomography applied to materials*," International Materials Reviews. **53** 129–181 (2008).

50. Y.J. Liu, P.P. Zhu, B. Chen, J.Y. Wang, Q.X. Yuan, W.X. Huang, et al., "*A new iterative algorithm to reconstruct the refractive index*," Phys. Med. Biol. **52** L5–L13 (2007).

51. Y. Ye, H. Yu, Y. Wei and G. Wang, "*A General Local Reconstruction Approach Based on a Truncated Hilbert Transform*," International Journal of Biomedical Imaging. **2007** 1–8 (2007).

52. A. Klug and R.A. Crowther, "*Three-dimensional Image Reconstruction from the VIewpoint of Information Theory*," Nature. **238** 435–440 (1972).

53. *"UCL Electrochemical Innovation Lab,"* https://www.ucl.ac.uk/electrochemical-innovation-lab (accessed November 7, 2015).

54. Panasonic, *"Notes and Precautions,"* http://industrial.panasonic.com/lecs/www-data/pdf/ACA4000/ACA4000PE1.pdf (accessed September 11, 2015).

55. Carl Zeiss X-ray Microscopy, Inc., Xradia Versa User's Guide, (Carl Zeiss X-ray Microscopy, Inc. Pleasanton, CA, 2014).

56. National Aeronautics and Space Administration, *"Limitations of Internal Protective Devices in High-Voltage/High-Capacity Batteries Using Lithium-Ion Cylindrical Commercial Cells,"* https://www.nasa.gov/sites/default/files/files/345992main_NESCTB09-02_LiIonBatteryLimitations.pdf (accessed October 2, 2016).